

# Reconstructing 15,000 years of southern France temperatures from coupled pollen and molecular (brGDGT) markers (Canroute, Massif Central)

5 Léa d'Oliveira<sup>1</sup>, Lucas Dugerdil<sup>1,2</sup>, Guillemette Ménot<sup>2</sup>, Allowen Evin<sup>1</sup>, Serge D. Muller<sup>1</sup>, Salomé Ansanay-Alex<sup>2</sup>, Julien Azuara<sup>3</sup>, Colline Bonnet<sup>1</sup>, Laurent Bremond<sup>1</sup>, Mehmet Shah<sup>4</sup>, Odile Peyron<sup>1</sup>

<sup>1</sup>Université de Montpellier, CNRS, IRD, EPHE, UMR 5554 ISEM, 34090, Montpellier, France

<sup>2</sup>Univ. Lyon, ENS de Lyon, Université Lyon 1, CNRS, UMR 5276 LGL-TPE, 69364, Lyon, France

<sup>3</sup>Université de Franche-Comté, CNRS, UMR 6565 Chrono-environnement, 25030, Besançon, France

<sup>4</sup>Université de Montpellier 3, UMR 5140 ASM, 334199, Montpellier, France

10 *Correspondence to:* Léa d'Oliveira (lea.d-oliveira@umontpellier.fr)

**Abstract.** Climatic changes in southern Europe during the Holocene are characterised by a strong spatial and temporal heterogeneity whose patterns are still poorly understood, notably the presence or not of a Holocene thermal maximum (HTM; 10,000–6,000 cal. BP). The climatic patterns also differ according to the proxies used (e.g., pollen, chironomid) and the latitude of the record. Here, a multi-proxy approach combining pollen and lipid biomarkers (branched Glycerol Dialkyl Glycerol Tetraethers, brGDGTs) is applied to the Canroute sedimentological sequence (Massif Central, France) to reconstruct the climatic variation over the last 15,000 years in southern Europe. This area is poorly documented in terms of vegetation and climate change. To provide reliable climate reconstructions, we have (1) performed a multi-method approach applied to pollen (MAT, WA-PLS, BRT and RF methods) and molecular biomarkers brGDGTs (5 calibrations), (2) investigated the role of modern databases/calibrations in climate reconstructions. Three different databases were tested for pollen data: one global based on a Eurasian Pollen Database, and two regional databases corresponding to Mediterranean/Temperate Europe and Temperate Europe/Scandinavian databases respectively. Five global calibrations were tested for lipid biomarkers including four for soil and one for peat. Results show that the use of different modern databases highlights the importance of considering environmental and ecological constraints when using transfer functions on pollen sequences. Pollen and brGDGT-inferred climate trends are consistent, notably for the Lateglacial, the Early and Late Holocene. However, the reconstructions notably differ concerning the presence of a Holocene thermal maximum with the Modern Analogue Technique (MAT) pollen-based method but not apparent with the BRT pollen method nor brGDGT. The temperature reconstructions estimated from the two independent pollen and lipid proxies are then compared to regional climate signals (chironomids, pollen, molecular biomarkers) to better understand global regional climatic patterns in South Europe. Altogether, our results from the Canroute sequence and those already available in southern Europe reveal that for the Lateglacial and Early Holocene, the regional climate trends are consistent between sites and proxies, supporting the reliability of their reconstructions despite some discrepancies. During the Holocene, the temperature signal of Canroute does not indicate the clear presence of a pronounced HTM, but rather stable temperatures.

15  
20  
25  
30

## 1 Introduction

The Holocene Epoch (last 11,700 cal. BP) is considered to be a stable climatic period compared to the previous Lateglacial period which corresponds to the deglaciation between *ca.* 15,000 and 11,700 cal. BP and alternating phases of rapid warming and cooling (Mayewski et al., 2004). However, the Holocene demonstrate regional climate oscillations at millennial and centennial timescales (Smith et al., 2016). In Europe, at a millennial scale, palaeoclimatological studies indicated the occurrence of a mid-Holocene thermic optimum called the “Holocene thermal maximum” (HTM) (Liu et al., 2014) dated between 10,000 and 6,000 cal. BP (e.g., Renssen et al., 2012; Marcott et al., 2013; Kaufman et al., 2020; Cartapanis et al., 2022). The temperature trends during this optimum show strong latitudinal patterns which differ between regions (Herzschuh et al., 2022). Marine proxies record an optimum in southern Europe and the Mediterranean region (Kaufman et al., 2020; Marriner et al., 2022), but this optimum is not clear for terrestrial proxies. Several studies suggest major differences according to region and latitude, as well as the proxy or seasonal parameter studied (Samartin et al., 2017; Erb et al., 2022). Pollen-based palaeoclimate studies have highlighted the Holocene climate heterogeneity in southern Europe and suggest for the mid-Holocene similar or cooler conditions than the current ones (Cheddadi et al., 1997; Davis et al., 2003; Mauri et al., 2015; Marsicek et al., 2018; Erb et al., 2022; Herzschuh et al., 2022). However, these climate patterns are not supported by atmospheric climate model outputs, which indicate a clear warming of northern and southern Europe during the Holocene (Mauri et al., 2014; Liu et al., 2014; Erb et al., 2022). This highlights the need for further palaeoclimatic studies in this region based on independent proxies, particularly in the southern Europe, for which the past climate remains poorly understood (Peyron et al., 2013; 2017; Samartin et al., 2017).

Terrestrial records provide especially useful information on climate change. However, terrestrial records can be influenced by environmental factors (e.g., erosion on detrital activity, elevation), which makes the responses of continental ecosystems to climate change difficult to interpret (Martin et al., 2020). Erosion has an impact on the detrital contribution to terrestrial archives; its dynamics are linked to, but not solely to, climate changes. Land clearing, for example, can increase detrital activity, and so impact the terrestrial record (van Andel et al., 1990). Peatlands are powerful environmental archives, used in palaeoecology for their capacity to conserve palaeoclimatic markers (Moore, 1989). The accumulation and preservation of pollen and other proxies in peatlands make it possible to reconstruct quantitatively variations in climatic parameters, such as mean annual/seasonal temperatures and/or precipitations (Salonen et al., 2019). Peatlands are particularly rich in organic matter, conducive to the presence of lipid biomarkers such as Glycerol Dialkyl Glyceryl Tetraethers (GDGTs) (Naafs et al., 2019), whose distribution and abundance are partly governed by environmental (e.g., pH) and climatic (e.g., temperature) factors, making them ideal proxies for palaeoclimatic reconstructions in the continental domain (Raberg et al., 2022). However, few research based on GDGTs have been conducted on the continental realm thus far, with the majority focused on lacustrine environments (c.f., Sun et al., 2011; Sinninghe Damsté, 2016; Russell et al., 2018).

In recent years, quantitative reconstructions of temperature based on brGDGTs were proposed both in marine and continental ecosystems (e.g., Schouten et al., 2013; Zheng et al., 2015, 2018; Ardenghi et al., 2019; Rodrigo-Gámiz et al., 2022; Dugerdil

et al., 2021a, b). Transmembrane lipids, synthesised by archaea or bacteria (Weijers et al., 2009; Pearson and Ingalls, 2013), have been identified in a wide range of environments including soils, peat, and lake and marine sediments (Hopmans et al., 2004; Weijers et al., 2006; Huguet et al., 2010; Pearson et al., 2011; Peterse et al., 2012; De Jonge et al., 2014a; Li et al., 2016; Naafs et al., 2017a, b). Two main families of GDGTs can be distinguished: isoprenoid GDGTs (isoGDGTs) and branched GDGTs (brGDGTs). Although the archaeal (*Thaumarchaeota*) origin of isoGDGTs has been validated, the brGDGTs source remains a subject of debate and investigation (Sahonero-Canavesi et al., 2021; Zeng et al. 2022). However, recent studies have shown GDGTs production in bacterial culture (Chen et al., 2022; Halamka et al., 2023) supporting a bacterial origin for brGDGTs. A relationship between the structure of biomolecules synthesised by organisms and environmental conditions to maintain cell viability has been demonstrated (Weijers et al., 2004; Naafs et al., 2021). More specifically, relationships between the degree of methylation and temperature (MBT) as well as between the degree of cyclization (CBT) and pH have been documented (Weijers et al., 2004, 2007). Furthermore, studies showed the presence of methyl isomers at the C6 position (6-methyl isomer), which when excluded from the MBT index resulted in the better temperature correlated MBT<sup>5Me</sup> index (Naafs et al., 2017a) and a novel C7 position (7-methyl isomer) that co-elute with the 5- and 6-methyl brGDGTs (Ding et al., 2016). De Jonge et al. (2019) revealed that brGDGTs had a varied relationship with temperature and pH in "warm" and "cold" bacterial communities, demonstrating that those correlations are also reliant on the bacterial population. A "community index" (CI ratio, De Jonge et al., 2019) has been defined to assess whether there is a change between the bacterial community and temperature or pH. De Jonge et al. (2019) determined a threshold value of 0.64 to separate the two groups of bacterial communities. If the CI ratio threshold is exceeded, a shift in the bacterial communities might be predicted, perhaps affecting the relationship between brGDGTs and temperature or pH (De Jonge et al., 2021). Furthermore, edaphic factors such as anoxic/oxic conditions have an impact on GDGT production and bacterial communities (Weber et al., 2018). Because crenarchaeol and GDGT-0 can be derived from Group I Crenarchaeota, the GDGT-0/Crenarchaeol ratio can be used to investigate the presence of methanogenic archaea that thrive in anoxic conditions in sediments, whereas methanogenic Archaea synthesize GDGT-0, but no crenarchaeol (Blaga et al., 2009). The lower the ratio, the lower the anoxic conditions. Indices and calibrations have been developed to allow quantitative reconstruction of palaeotemperatures based on archive type and region (Weijers et al., 2007; Peterse et al., 2012; De Jonge et al., 2014a; Naafs et al., 2017a, b; Dearing Crampton-Flood et al., 2020). These calibrations were developed from global databases that group together surface samples, for which the current climatic conditions are known, from distinct types of substrates: soils (Peterse et al., 2012; De Jonge et al., 2014a; Naafs et al., 2017a; Dearing Crampton-Flood et al., 2020), lake sediments (Russell et al., 2018; Martinez-Sosa et al., 2021; Raberg et al., 2021; Zhao et al., 2023) and peat (Naafs et al., 2017b).

The use of brGDGTs to reconstruct annual temperatures in Europe during the Lateglacial and/or the Holocene is still rare (e.g., Martin et al., 2020; Robles et al., 2023; Rodrigo-Gámiz et al., 2022; Ramos-Roman et al., 2022). Due to the complexity and number of interactions throughout each ecosystem (Birks and Birks, 2006), it is advisable to use several independent proxies to obtain reliable temperature reconstructions (e.g., Ponel et al., 2022). The general assumption is that all proxies used to reconstruct climate changes are to some extent dependent on climatic parameters, but other factors, including human activities,

100 biological processes, edaphic conditions, pH shift, and so on, can influence their distribution and/or abundance (Sugita et al.,  
2006; Huguet et al. 2010; Martin et al., 2020; De Jonge et al., 2021). In peat, this local environmental context can be understood  
through geochemical and sedimentary analyses based on X-ray fluorescence analysis (XRF) or loss on ignition (LOI), to  
investigate mineral inputs and organic matter content. However, the pollen record can also be influenced by anthropogenic,  
biological and environmental processes which can alter pollen production, dispersal, and preservation (Sugita et al., 2006).  
105 Production of molecular biomarkers, such as brGDGTs, may also differ depending on the source, edaphic parameters (e.g.,  
anoxic/oxic conditions), soil type and vegetation (Weber et al., 2018; De Jonge et al., 2021; Robles et al., 2022). Human  
activities, like deforestation and agriculture, can disturb the natural record of the vegetation-climate interaction, resulting in a  
biased quantitative reconstruction of climatic parameters from pollen data (Seppä and Bennett, 2003; Birks and Seppä, 2004).  
Furthermore, several studies document anthropogenic impacts on bacterial communities, demonstrating that reconstructions  
110 based on brGDGTs might be disrupted by human intervention in specific contexts, such as watersheds (Martin et al., 2019).  
In addition, due to the still significant calibration errors ( $\pm 3.8^\circ \text{C}$  to  $\pm 5.5^\circ \text{C}$ ), brGDGTs-based paleoclimate quantification  
should be interpreted with caution for periods with small temperature changes ( $< 2^\circ \text{C}$ ), as it is the case for the Late Holocene  
(last 2,000 years) (Naafs et al., 2019). In this sense, multi-proxy approaches are one of the best ways to estimate the reliability  
of quantitative climate reconstructions, as it is easier to disentangle local from regional events (Ponel et al., 2022). Although  
115 some studies compare palaeoclimatic reconstructions based on pollen and brGDGTs, allowing to reach complementary and  
more robust interpretations (Martin et al., 2020; Dugerdil et al., 2021a, b; Robles et al., 2022, 2023; Ramos-Roman et al., 2022;  
Watson et al., 2018), very few have been carried out on peat sequences; with none of them concerning southwestern Europe  
and the Mediterranean region nor covering the entire last 15,000 years.

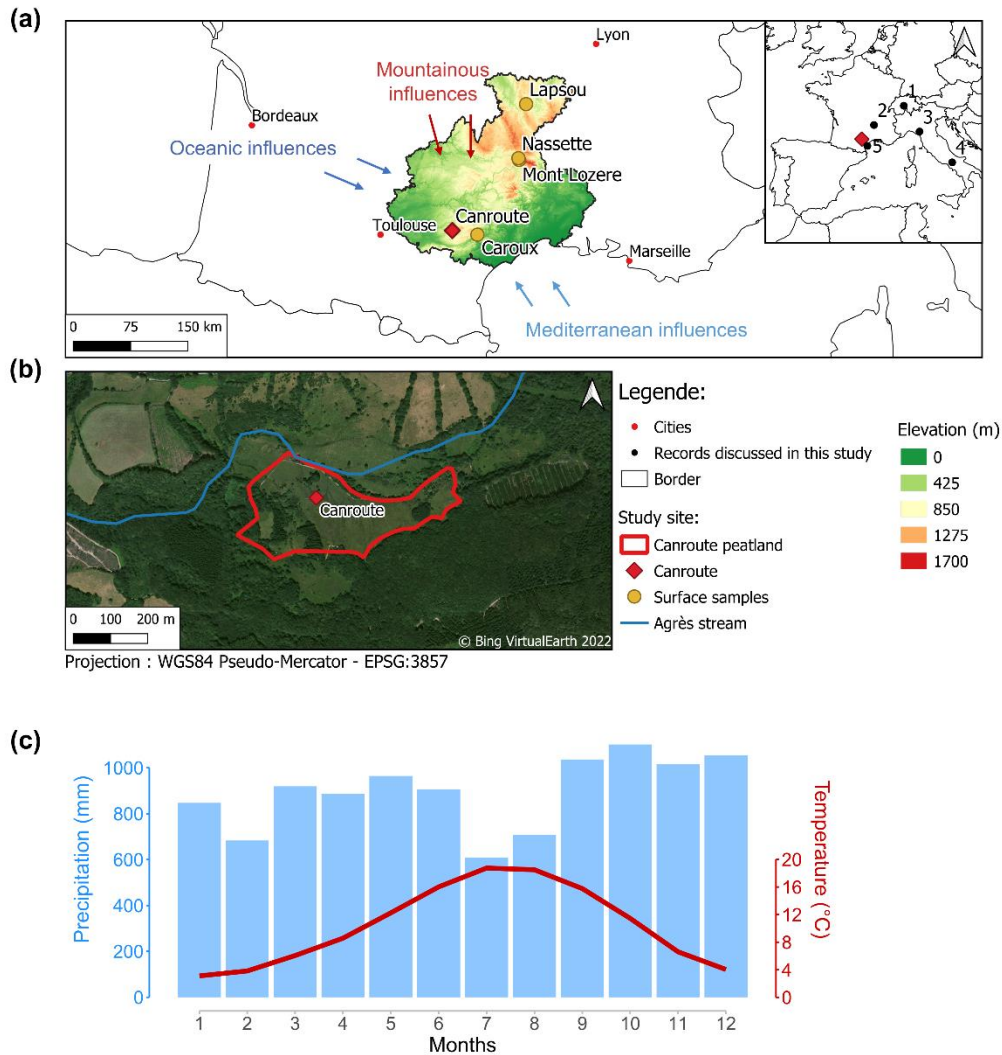
The aim of this study is (1) to address Holocene regional climate variability, within the context of the Holocene thermal  
120 maximum in southern Europe, from a peat sequence extracted in southern Massif Central (Canroute peatland) using a pollen-  
brGDGTs multi-proxy approach, (2) to contribute to palaeoclimatic reconstructions based on brGDGTs extracted from peat,  
which are still very little addressed in the field of biogeochemistry, and (3) to improve the reliability of the climate signal  
obtained from pollen data thanks to a multi-method approach (i.e., using four different methods including recent machine-  
learning as Boosted regression Trees) and the use of three modern pollen databases (regional to global).

## 125 **2 Material and methods**

### **2.1 Study area**

The Canroute peatland ( $43^\circ 38' 48'' \text{N}$ ;  $02^\circ 34' 35'' \text{E}$ ; alt. 790 m, Fig. 1a) is located in the south of the Massif Central (France),  
in the Monts de Lacaune. This soligenous *Sphagnum* peatland is supplied by several streams and small springs (Muller et al.,  
2018, Fig. 1b), and harbours a diversified vegetation including several species associated with the western Atlantic Ocean  
130 influence. The peatland is located at the confluence of three distinct climatic regimes: Mediterranean influence from the south,  
the influence of the Atlantic Ocean from the west due to Atlantic air masses arriving from the country's west coast, which are

not prevented by any topographical obstacles in the Aquitaine basin and mountainous one from the north (Fig. 1a). These influences result in an average annual temperature of 9.5°C, a temperature seasonality (TS, standard deviation of the monthly mean temperatures) of 0.5°C (WorldClim 2.0, Fick and Hijmans, 2017), higher summer temperatures, and an average annual rainfall of 895 mm with a slightly drier summer period (Fig. 1c, Table A1, CRU TS version 4.06, Harris et al., 2020) and a precipitation seasonality (SoP, standard deviation of the monthly precipitation) of 21 (WorldClim 2.0, Fick and Hijmans, 2017).



140 **Figure 1:** (a): Location and altitude of the Canroute peatland and modern surface samples (NASA JPL, 2013). Elevations of the samples departments (Aveyron, Gard, Hérault, Haute-Loire, Lozère and Tarn). The palaeoclimate records discussed in the text are represented by black dots in the inset map on the right (1: Swiss Alps, Heiri et al., 2003, 2: Lake St Front (Massif Central), Martin et al., 2020, 3: Lakes Gemini and Verdarolo (northern Apennines), Samartin et al., 2017, 4: Lake Matese (Italy), Robles, 2022a, 5: Gulf of Lion, Jalali et al., 2016). The southwestern Europe climate reconstruction provided by Davis et al. (2003) is based on numerous pollen-records (extracted from the EPD database) which are not shown for clarity. (b): Aerial view of Canroute Peatland. (c): Current annual conditions (precipitation and temperature) of Canroute (Monts de Lacaune).

## 2.2 Coring and sampling

The Canroute core (CAN02) extraction was carried out in 2019 using a 100 cm-long Russian corer. Two 100 cm sections were taken, spaced 20 cm apart, to cover a total depth of 169 cm.

150 Six peat-surface samples from the Massif Central were taken to refine the selection of calibrations for the reconstruction based on brGDGTs (Fig. 1a, Table A1).

## 2.3 Age-depth model

Radiocarbon dating of the CAN02 sequence was carried out by the Poznan Radiocarbon Laboratory (Poland) on 16 peat samples (bulk). The calibration and the age-depth model (Table 2, Fig. 2) were performed with the R language (R Core Team, 2022) and the R Studio software (RStudio Team, 2020) with the *Clam* package (Blaauw et al., 2022) using the IntCal20  
155 calibration (Reimer et al., 2020). No reservoir effects corrections were performed on the  $^{14}\text{C}$  measurements.

## 2.4 Sedimentological analysis

The CAN02 sequence was analysed by energy-dispersive X-ray fluorescence (ED-XRF) spectrometry using a Delta InnovX DP4000 portable spectrometer. The analyses were conducted on bulk sediments to preserve as much material as possible for other palaeoenvironmental studies. A three-beam “soil” analytical method was used, to measure the contents of trace elements  
160 (Pb, Zn, Rb, Sr, Zr, Ba) and of Ti. The element contents of Si, K, Ca and Fe were measured using a two-beam “mineral plus” analytical mode.

The organic matter content (OMC) was measured by loss on ignition (LOI) at 550°C (Ball, 1964). For this study, 16 samples of 1 cm<sup>3</sup> were taken every 10 cm. Each sample was weighed after drying for 12 hours at 150°C. Then, a calcination at 550°C for 5 h was performed to estimate the OMC (% of dry mass) (Decorsiere et al., 2019).

## 165 2.5 GDGT analysis and indexes

### 2.5.1 GDGT analysis

GDGT analysis was carried out in the LGLTPE-ENS laboratory in Lyon on 75 samples of the CAN02 core with a sampling step of 2 to 4 cm, and on the 6 surface samples (Fig. 1a). Sampling was carried out using a 1 cm<sup>3</sup> brass cutter (about 1g) and then were freeze-dried for 24 to 72 hours. After grinding and homogenisation, the total lipid fraction was extracted twice by  
170 microwave (MARS 6 CEM) at 70° C with 10 ml of dichloromethane (DCM)/methanol (MeOH) mixture (3:1, v/v) and then filtered on SPE cartridge. 1000 ng of C46 GDGT (99 % n-hexane: 1 % isopropanol) was then added to the Total Liquid Extract (TLE) to serve as an internal standard (Huguet et al., 2006). The TLE was then separated into polar and apolar fractions on a silica column with 5 ml of hexane/DCM (1:1), and 10 ml of DCM/MeOH (1:1) respectively. The samples were then analysed

in hexane/isopropanol (99.8:0.2) by high-performance liquid chromatography with mass spectrometry (HPLC-MS, Agilent 1200). Ions in Selected Ion Monitoring (SIM) are detected for mass-to-charge ratios ( $m/z$ ): 744 for the internal standard C46, 1302, 1300, 1298, 1296, 1294, and 1292 for isoGDGTs and then 1050, 1048, 1046, 1036, 1034, 1032, 1022, 1020, and 1018 for brGDGTs (Hopmans et al., 2016; Davtian et al., 2021). The high-performance liquid chromatography allowed for the separation of the 5-, 6- and 7-methyl brGDGTs isomers (Ding et al., 2016; Naafs et al., 2017a). Concentrations are expressed in  $\text{mg g}^{-1}_{\text{[sed]}}$ . The relative abundances of each GDGT (iso and br) are determined by the ratio of the proportion of the compound to the sum of all iso- or brGDGTs ( $n = 6$  and  $19$  respectively). Four samples with contrasting GDGT compositions were measured and integrated five times to establish the reproducibility of the analytical setup.

## 2.5.2 Indexes calculations

Different indices such as  $\text{MBT}'_{5\text{Me}}$ ,  $\text{CBT}_{5\text{Me}}$ ,  $\text{CBT}'$ , Index1, GDGT-0/Crenarcheol, IR (Isomer Ratio) and CI ratio (Community Index) were calculated for the CAN02 sequence and surface samples (Table 1). The mean annual temperature (MAAT) was reconstructed from three types of calibrations: the linear relationship between methylation indices ( $\text{MBT}'_{5\text{Me}}$ ) (De Jonge et al., 2014b; Naafs et al., 2017a) and Index1 (De Jonge et al., 2014b), multiple regression (mr) between MAAT and fractional abundances of selected brGDGTs (De Jonge et al., 2014b), and Bayesian (Dearing Crampton-Flood et al., 2020,  $\text{RMSE} = 3.8^\circ\text{C}$ ). Due to the removal of the pH-dependent 6-methyl brGDGTs,  $\text{MBT}'_{5\text{Me}}$  and Index1- based calibrations allow to overcome the substantial correlation between MBT and soil pH (De Jonge et al., 2014b). Multiple regression connects the MAAT with the fractional abundance of tetra- and penta-methylated brGDGTs and shows a little accuracy improvement over  $\text{MBT}'_{5\text{Me}}$ -based calibration (De Jonge et al., 2014b). Bayesian-based calibration permits to respect the intuitive reasoning of the relationship between  $\text{MBT}'_{5\text{Me}}$  and MAAT can be respected using Bayesian-based calibration (i.e., brGDGTs-producing bacteria respond to temperature changes, not the other way around) (Dearing Crampton-Flood et al., 2020). The Bayesian calibration employed in this study refers to Dearing Crampton-Flood et al. (2020)'s threshold-based calibration, which calibrates the  $\text{MBT}'_{5\text{Me}}$  index to the average temperature of all months with an average temperature above freezing. Changes in peat pH can have a significant impact on brGDGTs-based temperature, hence pH reconstruction based on brGDGTs, has been examined (De Jonge et al., 2021). The  $\text{CBT}'$ -based calibration was utilized (De Jonge et al., 2014b).

**Table 1: Formulae used for computation of brGDGT-indices, MAAT and pH calibrations and RMSE (in  $^\circ\text{C}$  for MAAT).**

Index	Formula	RMSE	Reference
$\text{CBT}_{5\text{Me}}$	$-\log_{10}\left(\frac{(\text{Ib} + \text{IIb}_{5\text{Me}})}{(\text{Ia} + \text{IIa}_{5\text{Me}})}\right)$	-	De Jonge et al., 2014a
$\text{CBT}'$	$\log_{10}\left(\frac{(\text{Ic} + \text{IIa}_{6\text{Me}} + \text{IIc}_{6\text{Me}} + \text{IIIa}_{6\text{Me}} + \text{IIIc}_{6\text{Me}})}{(\text{Ia} + \text{IIa}_{5-7\text{Me}} + \text{IIIa}_{5-7\text{Me}})}\right)$	-	De Jonge et al., 2014b

$MBT'_{5Me}$	$\frac{(Ia + Ib + Ic)}{(Ia + Ib + Ic + IIa_{5Me} + IIb_{5Me} + IIc_{5Me} + IIIa_{5Me})}$	-	De Jonge et al., 2014a
$Index1$	$\log 10 \left( \frac{(Ia + Ib + Ic + IIa_{6-7Me} + IIIa_{6-7Me})}{(Ic + IIa_{5Me} + IIc_{5Me} + IIIa_{5-7Me})} \right)$	-	De Jonge et al., 2014b
$III_a/II_a$	$\frac{IIIa_{5Me}}{IIa_{5Me}}$		Schouten et al., 2012
$GDGT - 0/Cren$	$\frac{GDGT - 0}{Crenarcheol}$		Blaga et al., 2009
$IR$	$\frac{IIab_{6Me} + IIIab_{6Me}}{IIab_{5Me} + IIIab_{5Me} + IIab_{6Me} + IIIab_{6Me}}$	-	De Jonge et al., 2021
$CI\ ratio$	$\frac{Ia}{Ia + IIa_{5Me} + IIIa_{5Me}}$	-	De Jonge et al., 2021
$MAAT_{Soil\ MBT'_{5Me}}$	$-0.8571 + 31.45 \times MBT'_{5Me}$	4.8	De Jonge et al., 2014b
$MAAT_{Bog\ MBT'_{5Me}}$	$52.18 \times MBT'_{5Me} - 23.05$	4.7	Naafs et al., 2017a
$MAAT_{Index1}$	$5.05 + (14.86 \times Index1)$	4.7	De Jonge et al., 2014b
$MAAT_{mr}$	$5.58 + 17.91 \times [Ia] + 25.9 \times [Ib] - 18.77 \times [IIa_{5Me}]$	5.0	De Jonge et al., 2014b
$pH_{CBT'}$	$7.15 + 1.59 \times CBT'$	0.52	De Jonge et al., 2014b

## 200 2.6 Pollen analysis and reconstruction of climate parameters from pollen assemblages

### 2.6.1 Pollen analysis

A total of 65 samples have been analysed (sampling interval of 1 cm for 159–138 cm, 2 cm for 138–128 cm, and 4 cm for 128–0 cm) and the pollen was identified and counted under an optical microscope under a light microscope at a standard magnification of  $\times 400$ . Pollen sums are at least 500 grains per sample and exclude spores. 148 taxa were identified, but here, a simplified pollen diagram was made to represent the vegetation variability over the last 15,000 years. The pollen data are presented as a function of age in years cal. BP (Fig. 6).

### 2.6.2 Quantitative reconstruction of climate parameters: a multi-method approach

Various methods have been developed to quantify climatic parameters from the pollen signal (see the review of Chevalier et al., 2020) and multi-method approaches have been developed to increase the reliability of palaeoclimatic reconstructions (Brewer et al., 2008; Peyron et al., 2005, 2011, 2013, 2017; Salonen et al., 2019; Robles et al., 2022, 2023). These methods were initially developed to calibrate the relationship between modern pollen data (soils, mosses) and current climate parameters. Our multi-method approaches include (1) transfer functions, based on linear regressions (Weighted Averaging Partial-Least Squares regression) between pollen taxa and climate parameters; (2) assemblage approaches, based on the analogy principle, between fossil and modern assemblages (Modern Analogue Technique), and (3) recent machine-learning



215 technics with regression trees (Random Forest and Boosted Regression Trees) to quantify the climate parameters on the CAN02  
sequence.

The Modern Analogue Technique (MAT), developed by Guiot (1990), is a method often used due to its simplicity of use,  
performance, and sensitivity. The MAT is based on measuring the degree of dissimilarity between a fossil pollen assemblage  
and modern pollen assemblages with known environmental characteristics to draw inferences about the temporal sequences of  
220 fossil samples with unknown environmental characteristics.

The WA-PLS method (ter Braak and Juggins, 1993) is a transfer function and is also a method often used; it assumes that the  
relationship between pollen proportion and climate is unimodal, where the abundance of a plant species is directly related to  
its environmental tolerance. WA-PLS estimates the climatic optimum of a species from calibration data by calculating the  
average climatological conditions in which a species occurs, weighted by the abundance of that species (Chevalier et al., 2020).

225 The other two methods (RF and BRT) have been developed more recently in palaeoclimatology and are based on Machine  
Learning (Salonen et al., 2019). These methods use regression trees to divide pollen data by successive separations of samples  
according to their abundance in the pollen spectrum. Random Forest (Breiman 2001; Prasad et al., 2006) is based on the  
estimation and combination of many regression trees, each tree is estimated from a set of pollen samples by bootstrapping  
(Chevalier et al., 2020). Boosted Regression Trees (De'Ath 2007; Elith et al., 2008) differ from RF in the definition of the  
230 modern database. For RF, each sample has the same probability of being selected, for BRT the under-represented samples in  
the previous tree have a higher probability of being selected. This approach is called “boosting” and increases the model's  
performance concerning the least well-predicted elements (Salonen et al., 2019). Due to the regression tree signal variation,  
the BRT method's final signal is an average of 15 independent runs of the BRT algorithm.

For these four methods, locals taxa and hydrophytes were not used in the reconstruction of climate parameters as they could  
235 not be strictly related to the regional climate.

The role of the modern pollen database in the reliability of climate reconstructions is also investigated here. The Eurasian  
Pollen Database (EAPDB, Fig. B1a), compiled by Peyron et al. (2013, 2017) and updated by Dugerdil et al. (2021a) was used  
as the first modern pollen database. In addition, two other modern pollen databases were used, originating from a sub-sampling  
of the EAPDB database, grouping sites from the Mediterranean and Temperate Europe (MEDTEMP, Fig. B1c) and sites  
240 originating from Temperate Europe and Scandinavia (TEMPSCAND, Fig. B1b). The temperatures reconstructed from those  
two sub-sampled databases are compared to the temperature reconstructed from the EAPDB (Fig. 7).

Here, we reconstruct the mean annual temperature (MAAT) from the Canroute pollen record as the MAAT is the only  
comparable parameter between pollen and brGDGT reconstructions. We also reconstruct the precipitations (MAP) to better  
discuss the links with the pH variations.

245 The reliability of pollen-inferred climate reconstruction methods was estimated by bootstrapping cross-validation by  
calculating the correlation coefficient values between the variables ( $R^2$ ) and those of the Root Mean Square Error (RMSE)  
criterion.

## 2.7 Statistical treatments

A principal component analysis (PCA) on correlation matrix has been conducted on XRF and brGDGTs, with the *FactoMineR* package (Le et al., 2008). The PCA aims to illustrate the components that explain the most variations across samples and thus permits to explore relationships between the variables. For both PCA, a k-means clustering allowed the highlight of subgroups in the data, with a chosen value of a cluster number ( $k$ ) determined with a within-cluster sum of squares method. The clustering analysis has been performed with the *Factoextra* package (Kassambara and Mundt, 2017). For XRF data used on for the PCA, due to the low detection signal of a part of the data, a regularized imputation of the missing values has been applied, using the *missMDA* (Josse and Husson, 2016) and *FactoMineR* (Le et al., 2008) packages. Missing values imputation reduces the loss of information caused by missing values, lowering the ability to discern patterns (Dray and Josse, 2014). Regularized imputation entails filling in missing values with values selected from a Gaussian distribution, with mean and standard deviation estimated from observed values (Josse and Husson, 2016). Additionally, element counts have been normalized over the Ti element (Davies et al., 2015).

Climate reconstructions and reliability tests ( $R^2$  and RMSE criterion) were performed with the *rioja* (Juggins and Juggins, 2020), *randomForest* (Breiman, 2001) and *dismo* (Hijmans et al., 2017) packages. All analyses were performed on R Studio (RStudio Team, 2020), using the *ggplot2* (Wickham, 2016) package for plots creation and the *rioja* package (Juggins and Juggins, 2020) for the pollen diagram with a CONISS hierarchy classification method described by Grimm (1987).

## 3 Results

### 3.1 Radiocarbon dating and age-depth model

**Table 2: Dating of the 16 samples of the Canroute core with mention of their depth in cm. AMS radiocarbon-dating and calibrated  $2\sigma$  age interval of the CAN02 core.**

Laboratory code	Depth (cm)	AMS $^{14}\text{C}$ (BP)	Age (cal. BP)
Poz-129948	19–20	$345 \pm 30$	480–310
Poz-109171	39–40	$3,150 \pm 35$	3,450–3,260
Poz-129949	59–60	$4,380 \pm 35$	5,040–4,860
Poz-141932	75–76	$5,120 \pm 40$	5,980–5,750
Poz-109172	79–80	$5,200 \pm 35$	6,160–5,900
Poz-142282	85–86	$5,640 \pm 40$	6,490–6,310
Poz-142283	95–96	$5,690 \pm 40$	6,620–6,360
Poz-129950	109–110	$5,710 \pm 35$	6,620–6,400
Poz-129951	119–120	$5,940 \pm 40$	6,880–6,670
Poz-109174	129–130	$6,710 \pm 30$	7,660–7,510

Poz-129995	139–140	7,830 ± 50	8,970–8,450
Poz-129996	149–150	9,790 ± 50	11,310–11,110
Poz-148568	154–155	9,900 ± 50	11,600–11,200
Poz-129997	159–160	11,620 ± 60	13,590–13,340
Poz-148570	164–165	11,720 ± 60	13,750–13,460
Poz-109175	168–169	11,070 ± 50	13,100–12,840

The CAN02 sequence covers the Lateglacial from *ca.* 15,000 cal. BP (171 cm depth) to -80 cal. BP (surface) (Fig. 2, Table 2).

270 The average accumulation rate is 0.01 cm yr<sup>-1</sup> between 170–113 cm, and 10 times higher between 110–85 cm (0.13 cm yr<sup>-1</sup>) with a maximum value of 0.18 cm yr<sup>-1</sup> at 95 cm depth (Fig. 2, shaded period). The accumulation rate drops back to initial values between 85–15 cm. It increases again to 0.03 cm yr<sup>-1</sup> from 15 to the core top.

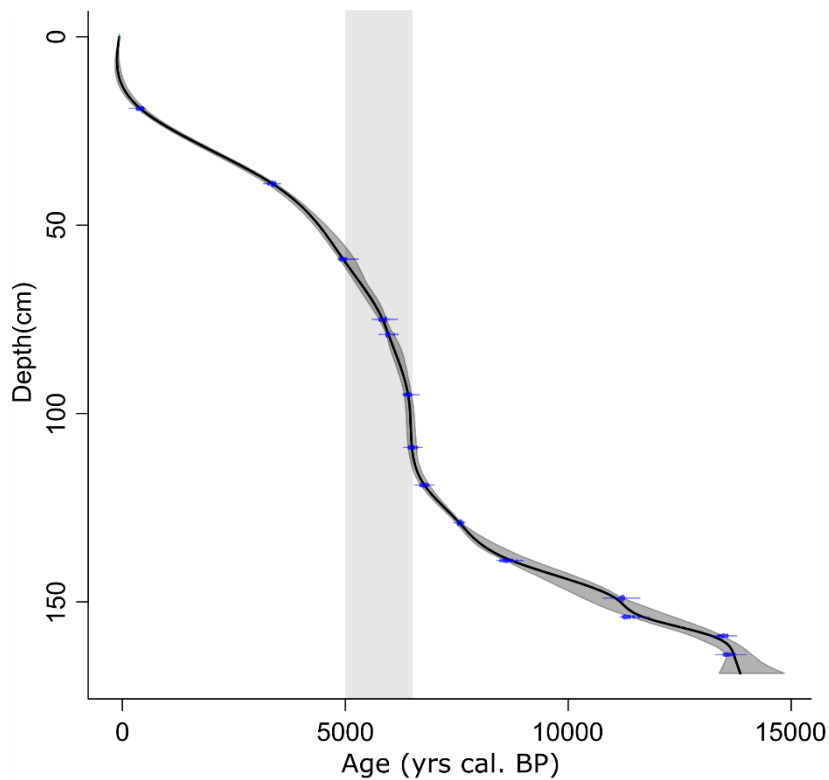


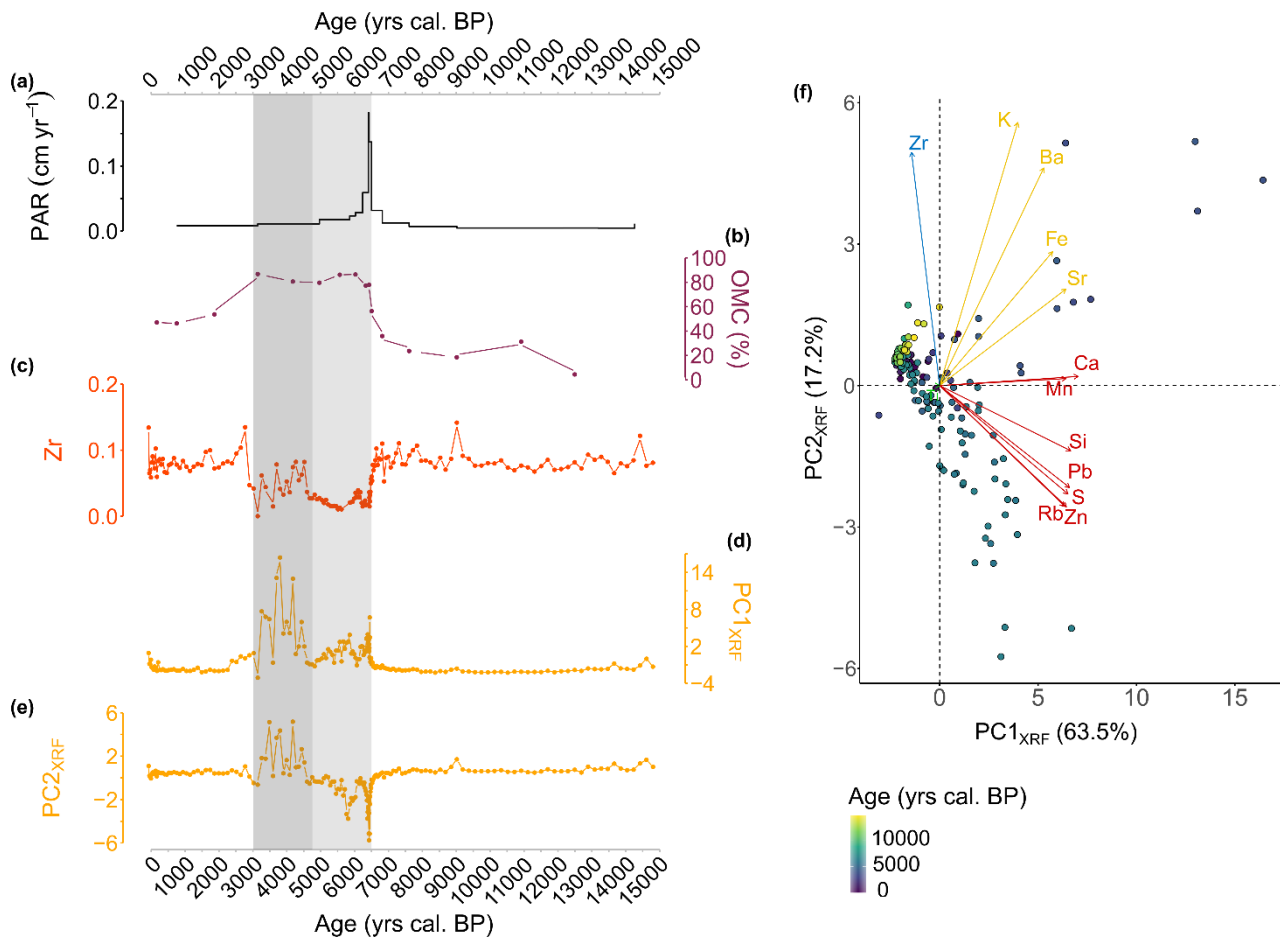
**Figure 2:** Age-depth model from the CAN02 sequence, built with Clam (Blaauw, 2022) on R (R Core Team, 2022). The shaded period corresponds to the interval of accumulation rate increase between 110 and 60 cm depth (6,500–5,000 cal. BP).

### 275 3.2 Sedimentological analysis

The peat accumulation rate (PAR, Fig. 3a) ranges from 0.01 to 0.18 cm yr<sup>-1</sup> with a maximum value between 6,500–6,340 cal. BP. The two first principal components PC1<sub>XRF</sub> and PC2<sub>XRF</sub> explain 63.5 % and 17.2 % of the total elemental variation (Fig. 3d, e). All elements are positively correlated with PC1<sub>XRF</sub>, except the Zr element. The PC2<sub>XRF</sub> illustrates two groups of

elements: elements such as Si, Pb, S, Zn and Rb on the negative side and Ca, Mn, Sr, Fe, Ba, K and Zr elements on the positive side (Fig. 3d, e). The Zr element (Fig. 3c) traces the detrital activity: the higher is the value, the higher are the lithogenic inputs (Silva-Sanchez et al., 2014). At Canroute, Zr element range from 0 to 0.14. High values of the Zr element are present from 15,000 to 6,600 cal. BP (0.05-0.14), revealing important detrital inputs, followed by a progressive lowering of detrital inputs. From 6,600 to 3,000 cal. BP, very low values of Zr are present (0–0.08), revealing the quasi-absence of detrital inputs. From 3,000 cal. BP onward, the values slowly increase to previous values (0.04–0.13), translating a recovery of detrital inputs.

285 The OMC estimated from the LOI (Fig. 3b) indicates low values (under 60 %) from 15,000 to 6,600 cal. BP. After this period, the OMC increases up to 90 % from 6,600 to 3,000 cal. BP after which it decreases to lower values (around 60 %). In more details, during from 6,600 to 3,000 cal. BP two dynamics are observed, highlighted by Zr element, PC1<sub>XRF</sub> and PC2<sub>XRF</sub> axes. The first dynamics extends from 6,600 to 4,700 cal. BP, during which the values of Zr element and both PC<sub>XRF</sub> axis are at their lowest and indicates a low variability (Fig. 3c, d, e, in light grey). The second dynamics extends from 4,700 to 3,000 cal. BP and is characterized by a higher values and variability in Zr elements and both PC<sub>XRF</sub> (Fig. 3c, d, e, in dark grey). During this 290 second period, the PC2<sub>XRF</sub> values becomes positive. Meaning that the origin of detrital inputs may have changed between the light and dark grey area.



295 **Figure 3: Geochemical data from the CAN02 sequence. (a):** Peat accumulation rate (PAR) calculated from the age-depth model (cm yr<sup>-1</sup>). **(b):** Organic matter content (OMC, %) derived from loss on ignition (LOI). **(c)** Zr relative counts, standardized on Ti element. **(d):** First dimension (PC1<sub>XRF</sub>) extracted from the principal component analysis (PCA) made on the XRF data. **(e):** Second dimension (PC2<sub>XRF</sub>) extracted from the principal component analysis (PCA) made on the XRF data. **(f):** Principal component analysis (PCA) of the XRF signal. The principal components are grouped into three clusters. Samples are coloured according to the age gradient (yrs cal. BP). On (a) to (e) shaded periods corresponds to the period between 6,600 and 4,700 cal. BP when the accumulation rate increases and detrital activity decreases (light grey period) and between 4,700 and 3,000 cal. BP when detrital activity increases and detrital input dynamics changes (dark grey period).  
300

### 3.3 GDGTs analysis

#### 3.3.1 Compound concentrations

In surface samples, the average concentrations of iso- and brGDGTs are  $0.6 \pm 0.5 \text{ mg g}^{-1}_{\text{[sed]}}$  ( $0.7 \times 10^{-6}$ – $0.4 \text{ mg g}^{-1}_{\text{[sed]}}$ ) and  $0.8 \pm 0.6 \text{ mg g}^{-1}_{\text{[sed]}}$  ( $0.9 \times 10^{-6}$ – $2.2 \text{ mg g}^{-1}_{\text{[sed]}}$ ), respectively. The CAN02 core samples have higher average concentrations of iso- and brGDGTs than the surface samples:  $2.1 \pm 2.0 \text{ mg g}^{-1}_{\text{[sed]}}$  ( $53.0$ – $1.5 \text{ mg g}^{-1}_{\text{[sed]}}$ ) and  $2.4 \pm 2.0 \text{ mg g}^{-1}_{\text{[sed]}}$  ( $143.6$ – $29.7 \text{ mg g}^{-1}_{\text{[sed]}}$ ), respectively.

### 3.3.2 Relative abundances

Average analytical errors are calculated from the averaged standard deviations of replicate measurements for br- and isoGDGTs (sd = 2 and 4 % respectively,  $n = 75$ ). Br- are predominant over isoGDGTs in the 7 surface samples (including CAN0) (average abundance of 92 % and 7 % respectively). IsoGDGTs of surface samples are dominated by GDGT-0 (between 47 % and 96 %, Fig. 4a). BrGDGT relative abundances in surface samples show the dominance of tetramethylated (Ia) and pentamethylated (IIa) (36 % and 37 % respectively, Fig. 4b). For CAN02 downcore samples, average relative abundances of iso- and brGDGTs show mean values of 12 % and 88 % respectively. Downcore samples are also dominated by GDGT-0 (isoGDGTs) and tetramethylated and pentamethylated (brGDGTs) (Fig. 4a, b). Double isomers are present in very low abundances and are present only between 7,800 and 6,420 cal. BP, at two occurrences for the IIIa<sub>7Me</sub> and one occurrence for the IIa<sub>7Me</sub>.

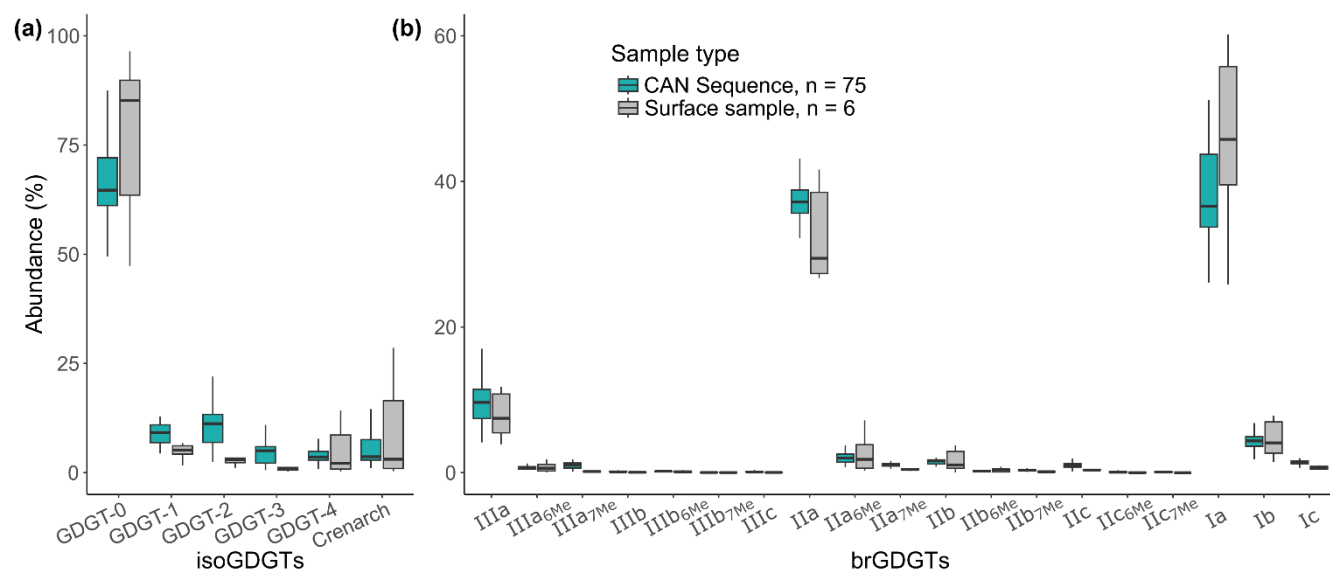


**Figure 4: GDGT results: Fractional abundances (%) of (a) isoGDGT and (b) brGDGT compounds for the CAN02 sequence ( $n = 75$ , blue) and surface samples ( $n = 6$ , grey).**

Penta- and hexamethylated brGDGTs show similar trends: a decrease between 15,000–6,600 cal. BP followed by an increase between 6,600–6,100 cal. BP and a further decrease between 6,100 and -80 cal. BP (Fig. 5a). Tetramethylated brGDGTs show the opposite trend: an increase between 13,800–6,600, followed by a sharp decrease between 6,600–6,300 cal. BP and then a gradual increase between 6,300 and -80 cal. BP. Pentamethylated brGDGTs dominate between 15,000–5,000 cal. BP, whereas tetramethylated brGDGTs dominate from 5,000 cal. BP onwards. The tetramethylated-dominated period can be divided in two subperiods both surrounded by lower values: 5,000-2,300 cal. BP and 2,300 cal. BP onward. The CBT' index ranges from -1.58 to -0.98 (sd = 0.05;  $n = 75$ , Fig. 5b), and shows a slight continuous decrease over time. The MBT'<sub>5Me</sub> index varies between 0.32 and 0.55 (sd = 0.01;  $n = 75$ ) and shows a slightly increasing trend over time (Fig. 5c), with two periods of rapid decrease

between 6,500–6,00 cal. BP and between 290 and -80 cal. BP and two well-differentiated periods: 15,000–6,500 and 4,700–290 cal. BP.

330 The Isomer Ratio (IR) values range from 0.03 to 0.13 with the lowest values obtained between 4,700 and 2,300 cal. BP (Fig. 5d). Throughout the record, the Community Index (CI) values range from 0.30 to 0.55 and are less than 0.65 (Fig. 5e). Period from 15,000 to 4,700 cal. BP has mean CI values of 0.38, but the period from 4,700 to -80 cal. BP has higher mean CI values of 0.49. The pH varies from 4.6 to 5.6 and shows a little continuous decline over time (Fig. 5f).

335 PCA on brGDGT relative abundances reveals that PC1<sub>brGDGTs</sub> and PC2<sub>brGDGTs</sub> account for more than 58 % of the variance in brGDGT compounds (PC1<sub>brGDGTs</sub> 45.6 %, PC2<sub>brGDGTs</sub> 13.1 %, Fig. C1b, c). The cluster analysis revealed three cluster (Fig. C1d), delimited by depth (cluster 1: 15,000-5,400 cal. BP; cluster 2: 5,400-2,300 cal. BP; cluster 3: 2,300-0 cal. BP), and demonstrated that the lower half of the sequence (cluster 1) is positively correlated with most brGDGT compounds (except Ia, Ib and Ic), while the upper half (cluster 2 and 3) is negatively correlated. That is, the lower half of the sequence (15,000-5,400 cal. BP) has a high abundance of most brGDGT compounds, whereas the upper half (especially 5,400-2,300 cal. BP) has a  
340 high abundance of primarily Ia.

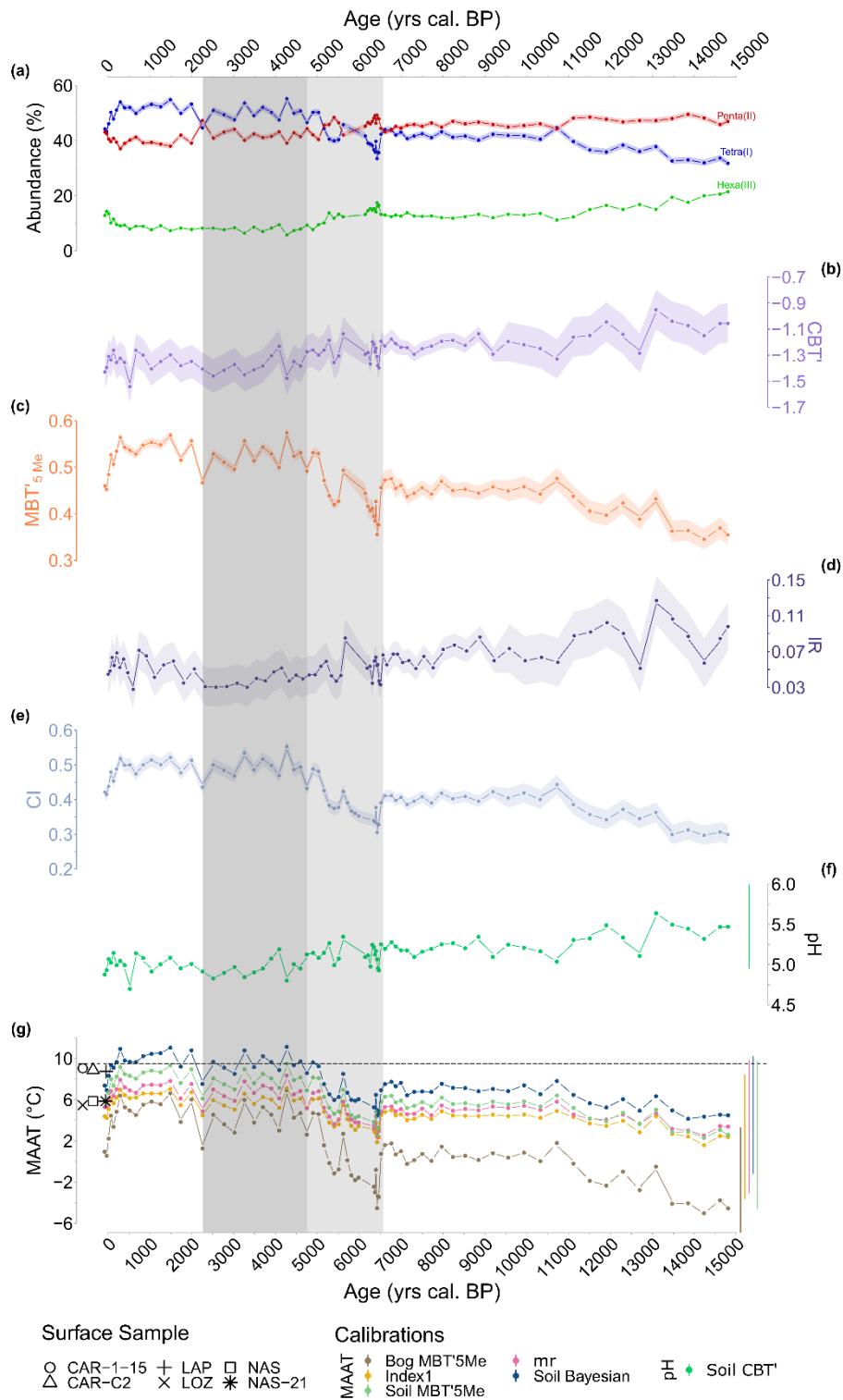


Figure 5: (a): Relative abundances of tetra-, penta- and hexamethylated brGDGTs in the CAN02 sequence. (b): Index of the degree



of cyclisation (CBT'). (c): Index of the degree of methylation (MBT'<sub>5Me</sub>). (d): Isomer Ratio (IR) through time. (e): Bacterial Community Index (CI) through time. (f): pH reconstruction based on global calibration of De Jonge et al., (2014a, Soil CBT'). (g): Annual mean temperature (MAAT) reconstructions based on global calibrations of De Jonge et al., (2014a, b) (Index1, Soil MBT'<sub>5Me</sub>, mr), Naafs et al., (2017a) (Bog MBT'<sub>5Me</sub>) and Dearing Crampton-Flood et al., (2020) (Soil Bayesian). Calibration errors are represented by the lateral lines on the right side. Shaded periods highlights the significant decrease in abundance of tetramethylated brGDGTs and a shift in accumulation rate from 6,600 to 4,700 cal. BP (light grey area) and the decrease in IR from 4,700 to 2,300 cal. BP (dark grey area). Symbols: modern MAATs of surface samples. Black dashed line: current calculated MAAT at Canroute.

### 350 3.3.3 Palaeotemperature reconstruction

All calibrations show similar trends during the Holocene, i.e. (1) cold conditions between 15,000–11,500 cal. BP, followed by (2) warmer conditions until 6,600 cal. BP (Fig. 5c). This stable period ends with (3) a drop in temperature between 6,600–5,000 cal. BP and is followed by (4) a new warming until 300 cal. BP, before (5) a new last drop in temperature (Fig. 5c). Despite similar and synchronous trends, the absolute values of temperature are different between calibrations. From the  
355 Lateglacial to the present, the peat calibration shows the lowest MAAT values, ranging from -5.0 to 6.9°C (sd = 0.5°C, n = 75) whereas multiple regression (mr), Index1, MBT'<sub>5Me</sub> and Bayesian calibrations are associated with higher MAATs values ranging from 1.59 to 11.51°C (sd = 0.3°C, n = 75). Among all calibrations, the multiple regressions, the Bayesian and the one based on Index1 shows the lowest variations (respectively 7.2, 6.9 and 5.5°C) compared to the peat calibrations and those based on methylation indexes (respectively 11.5 and 12.9°C).

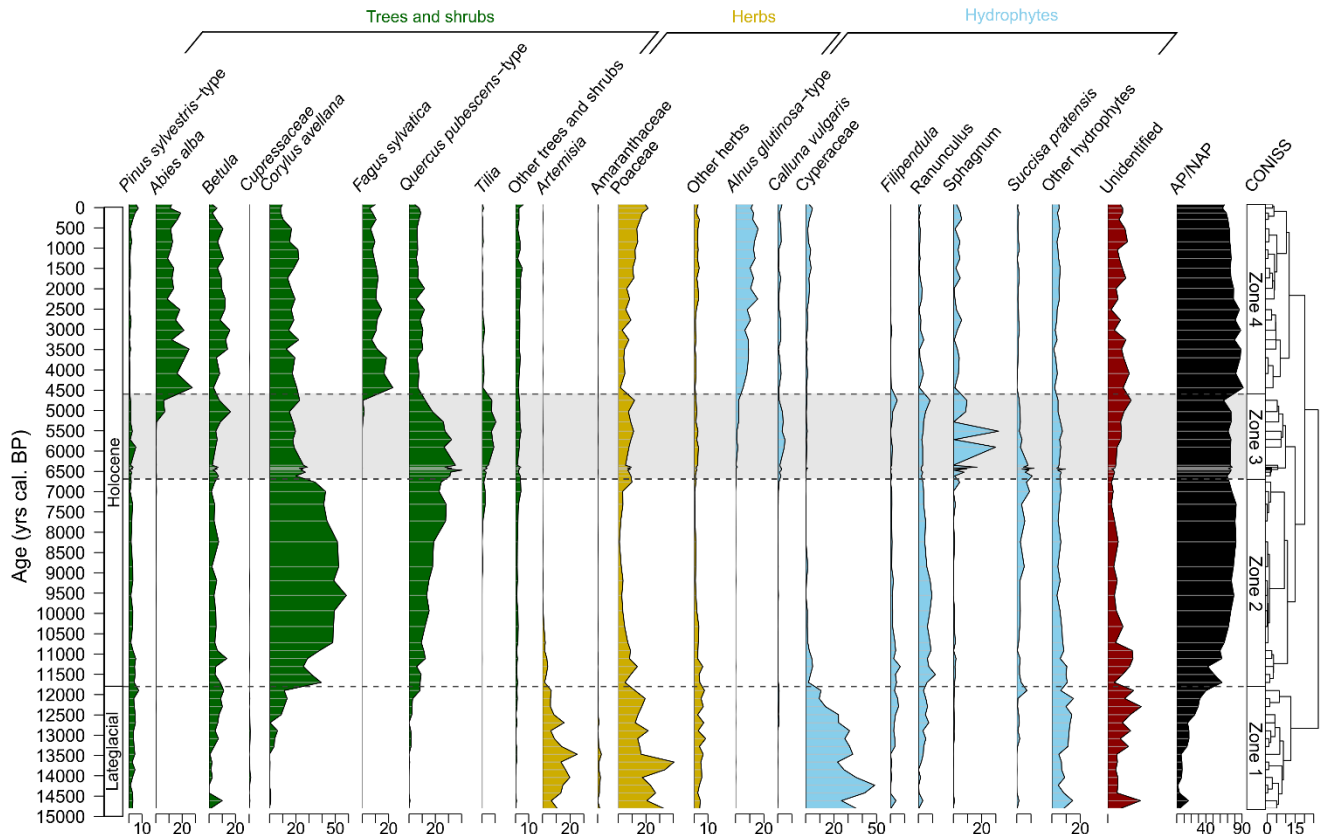
### 360 3.4 Pollen analysis

The Zone 1 (from 15,000 to ca. 11,700 cal. BP) of the pollen diagram (Fig. 6) is dominated by steppe taxa (*Artemisia*,  
Amaranthaceae, Poaceae), peatland (Cyperaceae up to 50 %) and megaphorbia (*Filipendula*, *Ranunculus*, *Succisa pratensis*),  
but contains some occurrences (mostly of long-distance origin) of *Betula*, *Corylus avellana*, *Pinus sylvestris*-type and *Quercus  
pubescens*-type. At the end of this period, the arboreal pollen represents ca. 45 % of the pollen sum, indicating the gradual  
365 replacement of the steppe vegetation by forests.

The Zone 2 (from 11,700 to 6,600 cal. BP) is dominated by *Corylus avellana* (up to 60 %), and to a lesser extent by *Quercus  
pubescens*-type (< 30 %) that progressively increases. During this period, the record of steppe taxa decreases, but hydrophytes  
are still present.

The Zone 3 (from 6,600 to ca. 4,500 cal. BP) is marked by an increase in *Quercus pubescens*-type and *Tilia* at the expense of  
370 *Corylus avellana*. This period is also marked by the decrease in megaphorbia taxa and by the record of Poaceae, *Calluna  
vulgaris* and *Sphagnum*.

Finally, the Zone 4 (from ca. 4,500 to -80 cal. BP) is characterised by the mesophilous *Abies alba* and *Fagus sylvatica*, and  
the hydrophyte *Alnus glutinosa*-type. *Corylus avellana* and *Quercus pubescens*-type continue to decrease, while *Tilia* is only  
slightly recorded.



375 **Figure 6: Simplified pollen diagram of the CAN02 sequence grouping selected tree taxa (green), herbaceous taxa (yellow), hydrophytes (blue) and AP/NAP ratio (black). Percentages were calculated on pollen sums excluding spores. The black dashed lines delineate 4 zones based on CONISS. The shaded period highlights the period of decrease in megaphorbia taxa to the benefit of *Calluna vulgaris* and *Sphagnum*(6,600–4,500 cal. BP).**

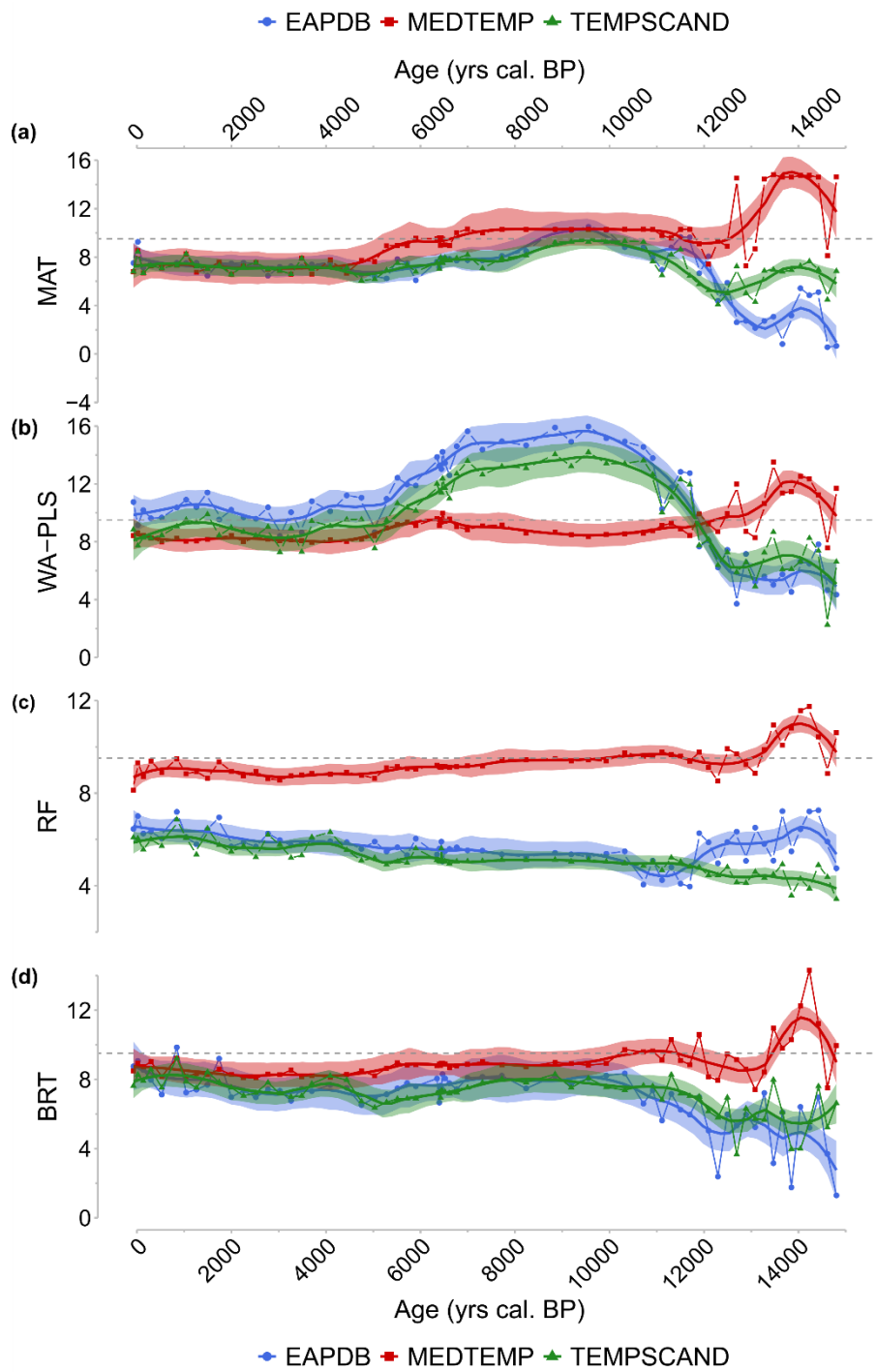
### 3.5 Pollen-inferred mean annual temperature

380 To provide reliable climate reconstruction, we applied to the Canroute pollen assemblages a multi-method approach tested here with three different modern pollen databases. The results based on the global EAPDB and regional TEMPSCAND databases indicate broadly the same temperature trends, but with smaller amplitudes for the TEMPSCAND calibration. The MEDTEMP regional calibration shows opposite trends compared to the other two databases, particularly during the Lateglacial (Fig. 7). The EAPDB and TEMPSCAND databases are associated with higher values of  $R^2$  than the MEDTEMP ones (Table 3).

385 3).

For the EAPDB and TEMPSCAND modern pollen datasets, three of the methods (MAT, WA-PLS and BRT) show a similar climatic signal (Fig. 7a, b, d) characterised by (1) cold temperatures during the Lateglacial, followed by (2) a warming through the Early Holocene, resulting in a thermic optimum accentuated depending on the methods used, then (3) a sudden cooling around 6,000 cal. BP, again followed by (4) a slight warming for 5,000 cal. BP onward. Cold conditions (MAAT around 2.3

390 to 8.7°C) are evidenced from 15,000 to 11,700 cal. BP. The first warming occurs between 11,700 and 6,000 cal. BP. The WA-  
PLS (and the MAT) indicate high values for this thermal optimum (Fig. 7a, b). While the BRT method indicates a warming of  
1.5° C between 12,000 and 6,500 cal. BP (Fig. 7d). The duration of the cooling observed around 7,000–6,500 cal. BP is method  
dependent. The cooling reconstructed with the MAT and WA-PLS is progressive with a variation in the MAAT of -2.1 and -  
4.5° C respectively and is shorter for the MAT than for the WA-PLS (Fig. 7a, b). The BRT indicates a slight cooling between  
395 6,400 and 4,700 cal. BP, less marked than for the other two methods, with a variation of -0.9° C (Fig. 7d). The last period is  
characterised by a slight warming trend particularly marked for the BRT and WA-PLS methods with an increase of +2.4 and  
+2.6° C respectively. The MAT indicate a warming of 1.9° C (Fig. 7c). BRT, MAT and WA-PLS are the three methods with  
the largest temperature amplitudes. The RF shows a much less contrasting climate signal over time (3.4° C variations between  
15,000 cal. BP and present, Fig. 7c), a climate pattern that is different than from the results obtained with the MAT, WA-PLS  
400 and BRT methods. Contrary to the EAPDB and TEMPSCAND, the results obtained with the MEDTEMP shows a warm  
Lateglacial and the absence of the thermic optimum for the four methods (Fig. 7).  
The BRT method shows higher values of  $R^2$  (Table 3,  $R^2 = 0.92$ ; RMSE = 1.30), and the RF method shows lower values of  $R^2$   
= 0.70 (RMSE = 1.83).



405 **Figure 7: Climate signal from the three calibration sets EAPDB (blue circles and curves), MEDTEMP (red squares and curves) and TEMPSCAND (green triangle and curve) for the MAT (a), the WA-PLS (b), the RF (c) and the BRT (d) methods. Black dashes: current MAAT at Canroute.**

410 **Table 3: Performance results of the MAT, WA-PLS, BRT and RF methods applied to three different modern pollen databases: the modern Eurasian (EAPDB), Temperate-Scandinavian (TEMPSCAND) and Mediterranean-Temperate (MEDTEMP) databases for mean annual air temperature (MAAT° C).  $k$  is the number of parameters used in the methods (e.g., number of analogues for the MAT method or the number of PLS components for the WA-PLS method). The best  $k$  corresponds to the number of parameters that infer the best  $R^2$  and calibration error (RMSE) values. The chosen  $k$  corresponds to the lowest number of parameters associated with the best  $R^2$  and RMSE values. In bold: Selected database and methods associated with their respective  $R^2$  and calibration error (RMSE) values.**

Database	Methods	Best $k$ $R^2$	Best $k$ RMSE	Chosen $k$	Chosen $R^2$	Chosen RMSE
EAPDB	MAT	4	6	4	0.87	3.09
	WA-PLS	3	3	3	0.71	4.11
	BRT	-	-	-	0.92	2.55
	RF	-	-	-	0.68	4.26
<b>TEMPSCAND</b>	<b>MAT</b>	3	6	3	<b>0.87</b>	<b>1.41</b>
	WA-PLS	3	3	3	0.60	2.14
	<b>BRT</b>	-	-	-	<b>0.92</b>	<b>1.30</b>
	RF	-	-	-	0.70	1.83
MEDTEMP	MAT	3	9	3	0.86	2.14
	WA-PLS	3	3	3	0.67	2.92
	BRT	-	-	-	0.91	2.02
	RF	-	-	-	0.74	2.45

## 4. Discussion

### 415 4.1 Past vegetation, peat accumulation and detrital activity

The Lateglacial steppe environment, dominated by *Artemisia*, Poaceae and to a lesser extent Amaranthaceae (including the ex-Chenopodiaceae), reveals cold and dry conditions. However, the record of Cupressaceae (only represented by *Juniperus* at that time) and especially *Betula* reveals the first afforestation dynamics supported by the slight warming of the Bølling-Allerød period. The end of the Lateglacial is characterised by the early expansion of temperate deciduous forests of *Corylus avellana* and *Quercus pubescens*-type, surprisingly contemporaneous with the Younger Dryas cooling event (12,900–11,700 cal. BP; 420 e.g., Broecker et al., 2010; Denton et al., 2010). Although the whole Younger Dryas is well recorded in northern regions (e.g., Duprat-Oualid et al., 2022), only the onset of the period is marked at Canroute by a peak of *Artemisia* and Amaranthaceae, and a punctual decrease in both *Corylus avellana* and *Quercus pubescens*-type. This pattern could be the result of a lack of accumulation, as the low PAR indicates during this period (Fig. 3a) or could be due to a not very marked Younger Dryas event 425 in this region.

The beginning of the Holocene is marked by a strong dominance of *Corylus avellana* that constituted woodland, whose open character can be associated with a dominant mechanic erosion of the soil (Mohammed et Adams, 2010), allowing the strong detrital activity revealed by XRF until 9,000 cal. BP. After this date, the progressive decrease in detrital activity may be attributed to the slow expansion of deciduous oaks, which replaced hazelnut open woodland across southern France and  
430 reduced the mechanic erosion. However, the slower establishment of dense deciduous forests compared to the southern Alps (de Beaulieu, 1977; de Beaulieu and Reille, 1983) suggests the influence of unfavourable climate conditions which slowed oak progression.

The emergence of a dense mature oak forest is attested between 6,600 and 4,500 cal. BP by both the maximal pollen record of *Quercus pubescens*-type and *Tilia* (Fig. 6), and the decrease in mineral input (Fig. 3b, c) that reveals the reduced detrital  
435 activity. Such a vegetation change occurring on the surrounding slopes is likely to have triggered hydrological changes within the studied wetland, which effectively experienced several contemporaneous changes: an abrupt acceleration of peat accumulation (Fig. 3a), an increase in organic matter content (from less than 40 % to more than 80 %; Fig. 3d; Joosten 2015) and a replacement of the previous megaphorbia by a bog-type peatland dominated by *Calluna vulgaris* and *Sphagnum* (Fig. 6). These changes are consistent with a loss of water runoff on the wetland surface, the result of either a reduced water supply  
440 resulting from a change in the river system or the natural rise of peatland surface that progressively isolated peat-forming vegetation from groundwater. Finally, change affecting both the local hydrophytic vegetation and the surrounding landscape occurs at ca. 4,500 cal. BP when the open peatland system is replaced by an alder swamp dominated by *A. glutinosa* (the only *Alnus* species present in the Massif Central), and the deciduous oak forest declines in favour of a mixed fir-beech forest. While this change could be interpreted as an environmental shift towards “mountainous” conditions, the contemporaneous pollen  
445 record of *Plantago* (not seen in Canroute) and the late-Neolithic date (Miras et al., 2004) could also suggest anthropogenic impact, which likely destabilised the competitive equilibrium in favour of the mixed forest onset.

## 4.2 Climate signal from pollen

Different studies underline the importance of the modern pollen database used for the reconstruction of climate parameters (Turner et al., 2021) and point out the advantage of regional calibration databases (Dugerdil et al., 2021a, b). The results  
450 obtained with the Eurasian pollen database (EAPDB) and regional Temperate and Scandinavian pollen database (TEMPSCAND) broadly indicate similar temperature trends at Canroute, while those based on the Mediterranean and Temperate pollen database (MEDTEMP) shows opposite trends (Fig. 7). These discrepancies can be explained by the dominance, at this period, of taxa such as *Artemisia*, *Amaranthaceae* and *Poaceae* (Fig. 6), able to constitute physiognomically and floristically similar arid steppes, both in the southern Mediterranean and Irano-Turanian warm context (e.g., Le Hou  rou,  
455 2001) and in the north-eastern Eurasian cold context (e.g., Yurtsev, 1982). From 11,700 cal. BP onwards, the methods performed on the three databases show similar trends but with different amplitudes. Signals obtained with the EAPDB and TEMPSCAND databases are particularly close, especially for the MAT and BRT methods (Fig. 7a,d) while climate results

based on the MEDTEMP dataset appear as non-reliable due to the absence of Mediterranean taxa in the pollen sequence (Fig. 6), as well as the poor  $R^2$  and RMSE values (Table 3).

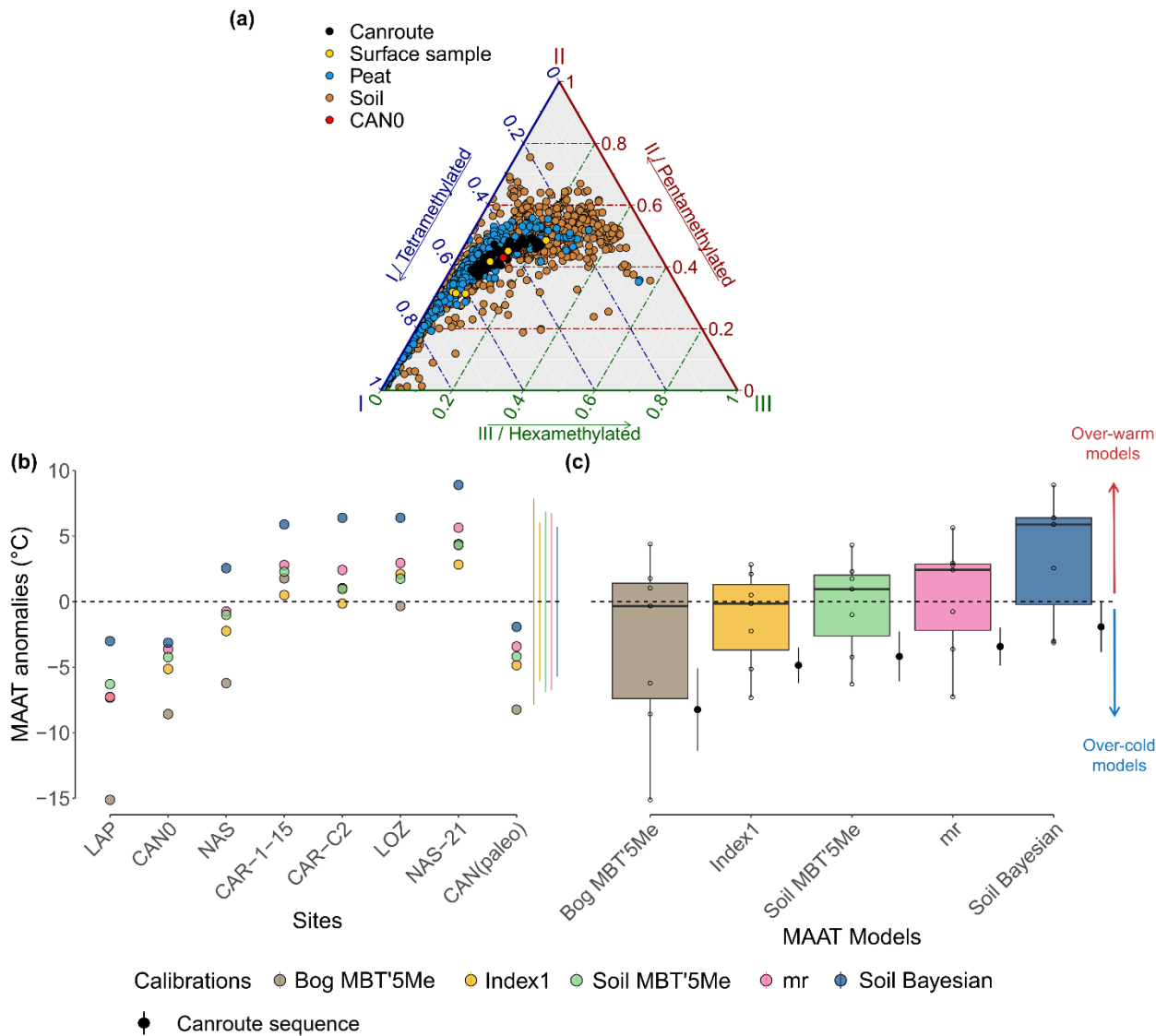
460 Among the four methods, RF and WA-PLS appear as the least reliable (low  $R^2$  and high RMSE, Table 3), so the MAATs reconstructed by these two methods will not be considered in the following discussion. For the MAT and BRT methods, the TEMPSCAND database calibration seems to produce a signal as reliable as the one produced with the EAPDB calibration set (close  $R^2$  and RMSE values, Table 3). The TEMPSCAND calibration produces a particularly close signal between the two methods, exhibits less variability and has better  $R^2$  and RMSE values, bolstering the reliability of the reconstructions based  
465 on this calibration database. Furthermore, calibrations employing regional datasets appear to be more reliable than those using global datasets (Dugerdil et al., 2021), and because the TEMPSCAND modern dataset is more regional than the EAPDB one, it will be taken into account in the subsequent discussion.

MAT and BRT are two methods based on different mathematical and ecological concepts (Chevalier et al., 2020), so their similar reconstructed trend supports the reliability of the methods and calibrations. However, the MAT shows a larger  
470 temperature range and in particular a slight thermal optimum in the Early Holocene, between 11,700–8,000 cal. BP (Fig. 7a). A similar pattern, although marked by more pronounced positive anomalies, is shown by Martin et al. (2020) for Lake St Front where high percentages of *Corylus* (< 55 %) are also recorded. Such a high proportion of *Corylus* does not exist in the modern pollen database assemblages of the TEMPSCAND dataset. The highest proportion (25–35 %) is associated with sites located in Italy, Ireland, and Albania, explaining the bias in the signal towards higher temperatures for the EAPDB- and  
475 TEMPSCAND-based calibrations. In the CAN02 pollen sequence, the Early Holocene is also characterised by high *Corylus* percentages (up to 60 %, Fig. 6), which could explain the large temperature variation between the Lateglacial and Early Holocene proposed by the MAT, the only method based on the similarity of present-day/fossil assemblages. For the 10,700–6,600 cal. BP period, it can be suggested that the MAT method is less efficient than the BRT one because Early-Holocene hazelnut woodland has no modern analogue. Nevertheless, both the MAT and BRT methods calibrated on the TEMPSCAND  
480 database can be retained in the following discussion because of the good reliability of their reconstructions.

### 4.3 Temperature signal from brGDGTs

#### 4.3.1 Consistency of brGDGTs relative abundances with peat and soils databases

The Canroute fossil samples and the surface samples from Massif Central are consistent with the global peat and soil databases that are globally dominated by tetra- and pentamethylated brGDGTs (Fig. 8a, Yang et al., 2014; Naafs et al., 2017a, b; Dearing  
485 Crampton-Flood et al., 2020). The use of both types of calibrations (peat and soil) therefore appears to be consistent with the brGDGT assemblages observed in the CAN02 sequence.



490 **Figure 8:** (a) Ternary plot of fractional abundances of tetra-, penta- and hexamethylated brGDGTs for CAN02 core samples (in black) and Massif Central surface samples (in yellow and red); and for global peat (Naafs et al., 2017b, in blue) and soil databases (Yang et al., 2014; Naafs et al., 2017a; Dearing Crampton-Flood et al., 2020, in brown). (b, c): Testing of soil and peat calibrations on surface samples and CAN02 core samples. (b): Reconstructed MAAT from each calibration expressed as anomalies with respect to the mean annual temperatures measured at the sites. The standard deviation of each calibration applied to the CAN02 sequence (paleo) is represented by the lateral lines on the right side. (c): Boxplot representing the results of the calibrations applied to the surface samples ( $n = 6$ ). Black points with error bars next to each calibration correspond to temperature anomalies of CAN02 core samples.

495

### 4.3.2 Selection of the most relevant brGDGT-calibrations

The brGDGT relative abundances in the surface samples of Nassette (NAS), Lapsou (LAP) and Canroute (CAN0) are close to that of the Canroute (CAN02) sequence. For these three samples, the Bayesian calibration (Soil Bayesian, Dearing Crampton-



Flood et al., 2020), the one based on MBT'<sub>5Me</sub> (Soil MBT'5Me), Index1 (Index1) and multi-regression (mr) (De Jonge et al., 2014b) show more reliable reconstructed MAAT anomalies compared to the current MAAT of their respective location (Fig. 8b). For the samples from the Caroux site (CAR-1-15 and CAR-C2), which is also a soligenous peatland and is geographically the closest site to Canroute (Fig. 1a), the calibrations based on Index1, and multi-regression appear to be the most reliable compared to their current MAAT (Fig. 8b). For the Canroute surface sample (CAN0), the calibration based on the MBT'<sub>5Me</sub> (Soil MBT'5Me) and the Bayesian calibration (Soil Bayesian) provides temperature values closer to the present temperatures at Canroute (Fig. 8b). Soil calibrations based on Index1, MBT'<sub>5Me</sub>, multi-regression and Bayesian calibration produced the most suitable MAATs: both the Index1 and the multi-regression calibrations show a good estimate of the current MAAT, with a low scatter and a current MAAT close to the observed climatic conditions at Canroute (Fig. 8c). When applied to the whole sequence (CAN02), these two calibrations (Index 1 and mr) have the lowest standard deviations (respectively  $sd = 1.4^{\circ}C$  and  $1.5^{\circ}C$ ;  $n = 75$ , Fig. 8c). Regarding the Bayesian and MBT'<sub>5Me</sub> calibrations, they show a less reliable estimate of the current MAAT and have close standard deviation when applied to the CAN02 sequence ( $sd = 1.9^{\circ}C$ ;  $n = 75$ , Fig. 8c). However, the Bayesian calibration is associated with a lower error than the MBT'<sub>5Me</sub> based one (RMSE =  $3.8^{\circ}C$  and  $4.8^{\circ}C$  respectively, Fig. 8b).

Ultimately, among the 5 calibrations tested, 3 of them (Bayesian, Index1 and mr) are retained for the interpretation of the climate trend at Canroute, due to the low RMSE of the Bayesian calibration and the low standard deviations of Index1 and multi-regression (mr) calibrations reconstruction.

### 4.3.3 Interpretation of the climate signal

According to various studies in peatlands, communities of brGDGT-producing bacteria as well as brGDGT composition are controlled by local hydrological conditions (Rao et al., 2022), vegetation composition (Xiong et al., 2016) and pH (De Jonge et al., 2021), whose changes are thus likely to affect temperature reconstructions (De Jonge et al., 2019). Furthermore, edaphic factors such as anoxic/oxic conditions have an impact on GDGT production and bacterial communities (Weber et al., 2018). Because crenarchaeol and GDGT-0 can be derived from Group I Crenarchaeota, the GDGT-0/Cren ratio can be used to investigate the presence of methanogenic archaea that thrive in anoxic conditions in sediments, whereas methanogenic Archaea synthesize GDGT-0, but no crenarchaeol (Blaga et al., 2009). The lower the ratio, the lower the anoxic conditions. Crenarchaeol is also an indicator of the water-table level, which refers to the limits between the acrotelm and catotelm in peatlands, and therefore is an indicator of anaerobic conditions (Yang et al. 2019). In the CAN02 sequence, the abundance GDGT-0 decreases in favour of Crenarchaeol over time (Fig. C1a). This points to less anoxic conditions, indicating that the Canroute water-table level lowers over time, making the peatland surface drier. Furthermore, the brGDGTs index IIIa/IIa, which investigates brGDGTs sources (Xiao et al., 2016), exhibits a significant shift in its values throughout the sequence (0.12 to 0.46), demonstrating the effect of environmental change on brGDGTs composition. This correlates well with other proxies such as geochemical and pollen data that evidence a hydroseral succession from a water-demanding megaphorbia to peatland and alder-swamp plant communities. Past vegetation and detrital activity showed the presence of three different local conditions

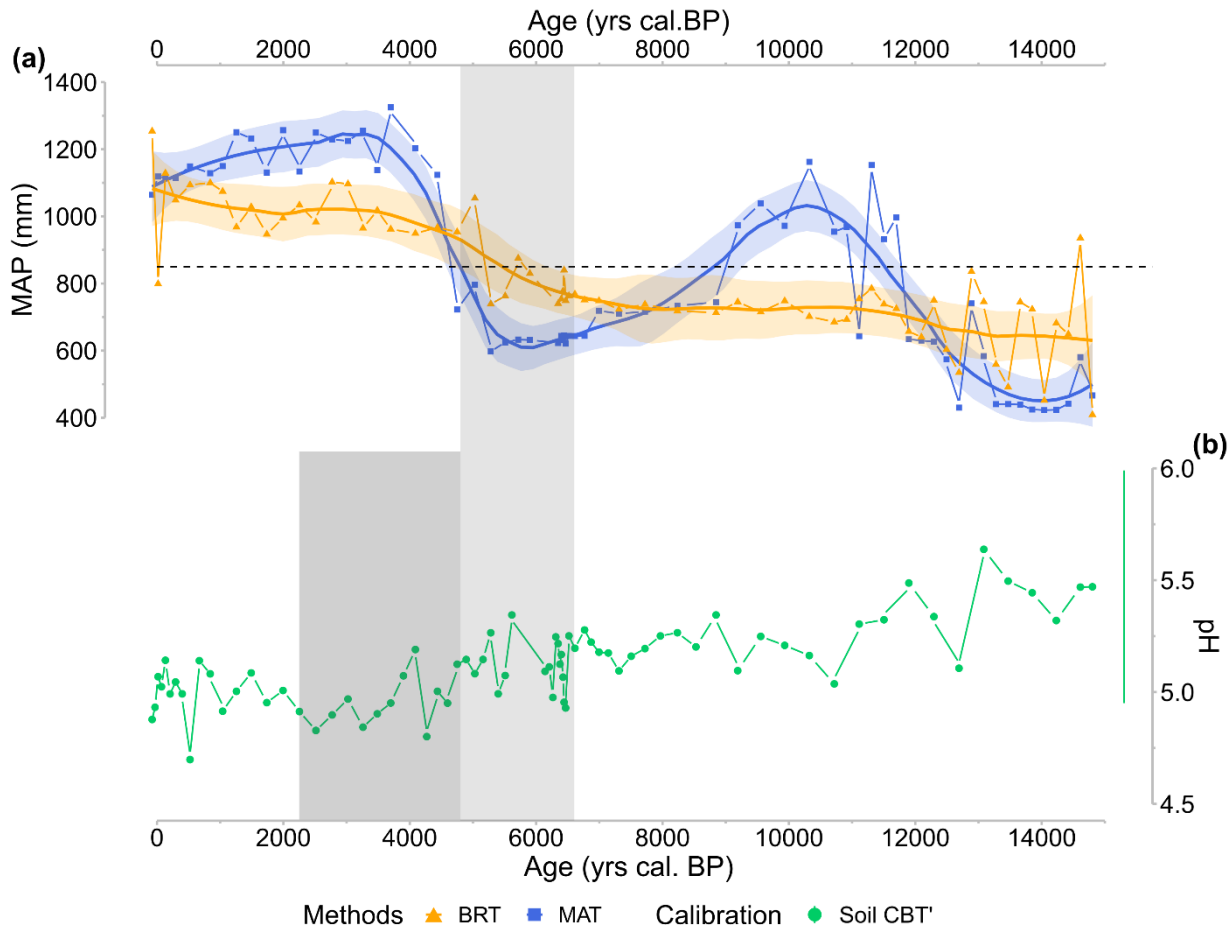
in the peat, which can result in large pH fluctuations because plants influence soil and peat pH (De Jonge et al., 2021). Changes in pH can alter the fractional composition of brGDGTs and the bacterial community, influencing the MBT'<sub>5Me</sub>-based temperature. CBT' and IR show the increase of 6-methyl brGDGTs as pH increases. IR and CBT' values in the CAN02 sequence are at their lowest from 5,000 to 2,300 cal. BP (Fig. 3b, Fig. 5d, dark grey shaded area), resulting in a modest decrease in pH values (Fig. 3e). There is no change in the MBT'<sub>5Me</sub> during this time period, indicating that the change in brGDGTs composition has no effect on the MBT'<sub>5Me</sub> employed for the temperature quantification. Soil/peat pH is also related to global climate patterns via precipitation, meaning that changes in precipitation dynamics over time might cause pH variations (De Jonge et al., 2021). Pollen-based precipitation changes (MAP) at Canroute can be confronted to brGDGTs-based pH reconstruction to try to differentiate the effects of climate and bacterial communities on pH variation (Fig. 9). The same methods and calibration as MAAT were utilized for the MAP signal, namely the BRT and MAT methods with the TEMPSCAND calibration. The MAP and pH signals do not appear to correspond well, as the wettest periods (from 11,500-8,500 cal. BP and 4,500 cal. BP onwards) are not associated with a noticeable decrease in pH (Fig. 9). This shows that precipitation dynamics have little effect on pH in Canroute peatland. Precipitations, which are normally acidic can cause a low pH in ombrotrophic peatland (water supplied primarily by precipitation) (Sennès, 2004). Canroute, on the other hand, is a soligenous peatland, and because most of its water supply originates from streams and springs (Julve, 1994), its local vegetation is less affected by precipitation dynamics. This shows that pH variations are produced mostly by local vegetation and detrital changes, which are influenced by local hydrological conditions.

Temperature reconstructions can be affected by changes in the bacterial community of brGDGT producers (De Jonge et al., 2019) which can be studied using variations in CI values (De Jonge et al., 2021). Although the CI values in the CAN02 sequence do not exceed the 0.65 thresholds established by De Jonge et al. (2021), a significant shift in value indicates a potential change in bacterial community composition from 6,600 to 4,700 cal. BP (Fig. 5e), implying that the temperature interpretation during this period should be done with caution.

Dearing Crampton-Flood et al. (2020) used two indicators of the presence or absence of climate seasonality, in terms of precipitation (SoP) and temperature (TS), to investigate a possible bias in the production of brGDGT compounds. The SoP index can aid in interpreting whether a region presents a potential production bias due to variability in the timing of precipitation (Dearing Crampton-Flood et al., 2020). A low SoP value is indicative of a relatively constant MAP through the year. Canroute is associated with a low SoP value (21) and therefore does not show a heterogeneous precipitation pattern, which can create a bias in the production of brGDGTs. A region associated with a TS value over 20 is considered to have high-temperature seasonality, which biases the proxy toward summer temperatures (Dearing Crampton-Flood et al., 2020). At Canroute, the TS value results in monthly mean temperature variability under 20° C which indicates a low-temperature seasonality, without bias.

Consequently, the climate signal reconstructed by brGDGTs does not seem to be drastically impacted by the changing environmental context before and after the 6,500–4,700 cal. BP period. However, during the 6,500–4,700 cal. BP period, the shift from a running water-demanding vegetation to a less-demanding one (Fig. 6) seems to induce a shift in brGDGT indexes

and bacterial communities. The temperature values reconstructed for this period (Fig. 5g, light grey shaded area) thus must be interpreted with caution.



570 **Figure 9: CAN02 (a) pollen-inferred reconstructions of the annual precipitation (MAP, in mm) obtained with BRT (yellow squares and curve) and MAT (blue triangles and curve) methods based on the TEMPSCAND calibration. The solid line corresponds to locally estimated scatterplot smoothing (loess) regression curves, the shaded area corresponds to its 95 % confidence interval. The black dashed line corresponds to Canroute's current calculated MAP. (b) CBT'-based pH reconstruction (green circles and line, De Jonge et al., 2021). On the right, the lateral line represents calibration error (RMSE). The time highlighted in light grey reveals a large fall in tetramethylated brGDGT abundance and a shift in accumulation rate (6,600–4,700 cal. BP) and a shift in accumulation rate.**  
 575 **The era shown in dark grey highlights the decrease in CBT' and IR values (4,700–2,300 cal. BP).**

#### 4.4 Temporality of proxies' resilience to environmental changes

There are two distinct periods for which proxy records are impacted by environmental influences, notably a hydrological change in the peatland (Figs. 3, 6, shaded areas). The record of vegetation (Fig. 6), detrital signal (Fig. 3) and brGDGT compounds (Fig. 5) all show a first response to a loss of water runoff on the wetland surface between 6,600–4,700 cal. BP, the  
 580 result of either a reduced water supply from a change in the river system or the natural rise of peatland surface that gradually

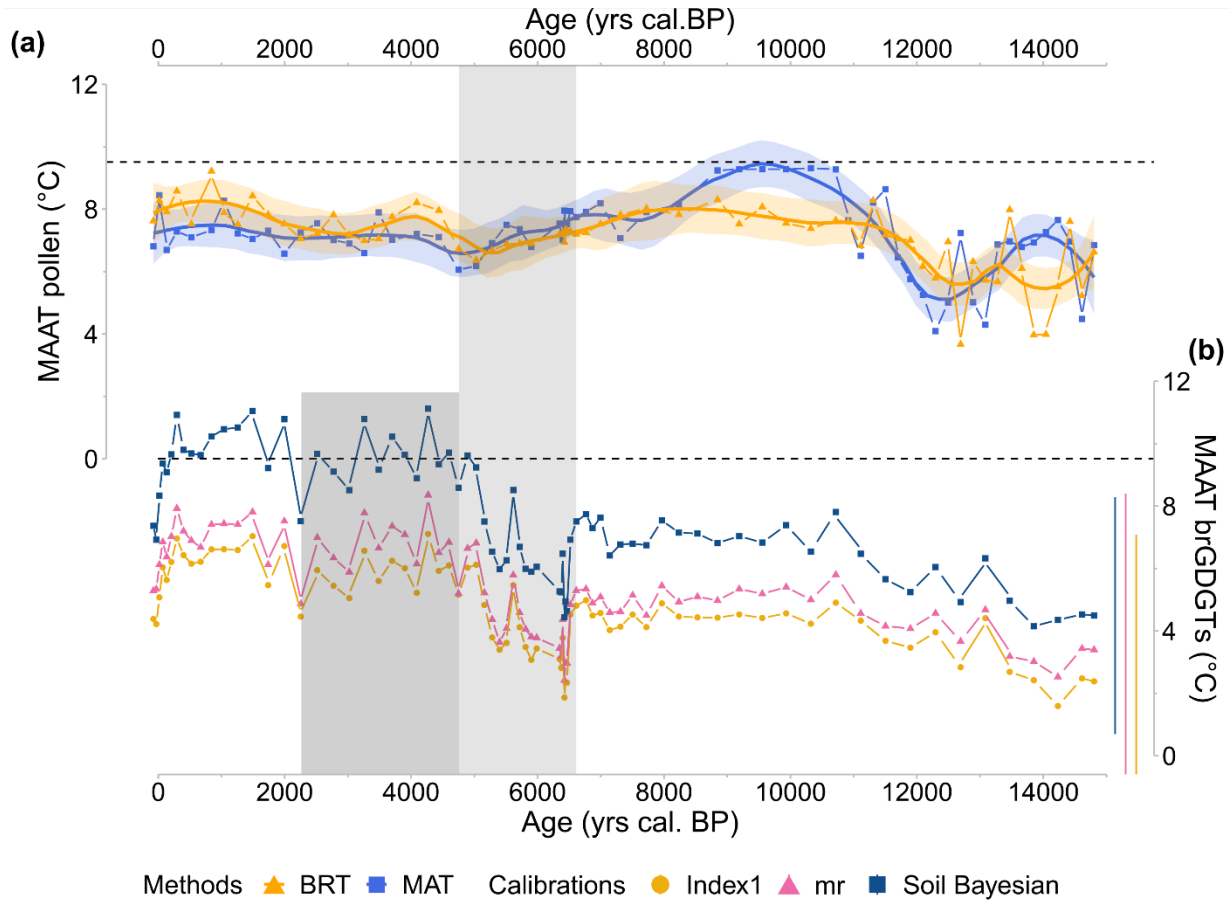
isolated peat-forming vegetation from groundwater. Two of the three proxy (detrital signal and brGDGT compounds) exhibit a second response to the hydrological shift between 4,700 and 3,000 for the detrital signal and 2,300 cal. BP for the brGDGT compounds (Figs. 3, 5, C1, dark grey area). To explain the timing in the proxies' responses to environmental changes, a distinct resilience, depending on the proxy, might thus be postulated. Walker (2004) defines resilience as the system's ability to absorb disturbance and reorganize while experiencing change in order to retain essentially the same function, structure, identity, and feedback. In this study, vegetation appears to be more resilient than the detrital signal and brGDGT compounds, returning to equilibrium faster. Both the sedimentological and brGDGT signals demonstrate, a synchronous reaction to vegetation, as well as a second response after the vegetation is back to equilibrium. Furthermore, brGDGTs appear to have less resilience than sedimentological signals because the return to equilibrium is not recorded before 2,300 cal. BP, whereas the detrital signal is recorded before 3,000 cal. BP. However, it is unknown if this second response to environmental changes affects brGDGTs distribution and bacterial community composition.

#### **4.5 Temperatures changes in the northern Mediterranean basin since the Lateglacial: a synthesis**

##### **4.5.1 Local climate from the CAN02 record based on two independent proxies**

The temperatures inferred from pollen data (BRT method, TEMPSCAND modern database) and brGDGT data (Bayesian, mr and Index1 calibrations) show very similar trends through the Holocene (Fig. 10). During the Lateglacial, cold conditions are evidenced from 15,000 to 11,700 cal. yrs BP followed from 10,500 to 6,600 cal. BP by warmer conditions (plateau) with temperatures lower than those observed today. Contrary to the BRT and brGDGT signal, the MAT method based on the TEMPSCAND modern database shows a slight thermic optimum from 10,500 to 8,000. After the thermic optimum, the onset of a cooling trend until 6,600 cal. BP is evidenced (Fig. 10a). Due to a possible bias during the shaded area, the 6,600 – 4,700 cal. BP period will not be discussed. From 4,700 to 200 cal. BP, a slight warming trend is reconstructed for both proxies. Finally, from 200 cal. BP onward, an abrupt cooling characterizes the brGDGT signal (Fig. 10b), while the pollen signal shows only a slight cooling trend (Fig. 10a).

605 Early to Mid-Holocene temperatures cooler than the present-day ones and followed by a Late-Holocene warming (i.e., the inverse of the HTM followed by a Late-Holocene cooling), inferred by two independent proxies, appear as a robust reconstruction of mean annual temperatures for Canroute. This climate pattern is consistent with both atmospheric climate model outputs (Mauri et al., 2014; Liu et al., 2014; Wanner et al., 2021; Erb et al., 2022) and pollen-based palaeoclimatic studies (Herzschuh et al., 2022), which depicted the absence of a thermic optimum for the same latitudes. According to several studies, the presence of the HTM can result from a seasonality bias toward summer temperatures (Liu et al., 2014; Samartin et al., 2017; Wanner et al., 2021; Herzschuh et al., 2022).



610 **Figure 10: CAN02 temperature reconstructions (MAAT, in °C) obtained from (a) pollen assemblages using BRT (yellow triangles**  
 615 **and curve) and MAT (blue squares and curve) methods based on the TEMPSCAND calibration. The solid line corresponds to locally**  
**estimated scatterplot smoothing (loess) regression curves, the shaded area corresponds to its 95 % confidence interval, and (b)**  
**brGDGT signal for the three selected soil calibrations: Soil Bayesian (dark blue squares and line, Dearing Crampton-Flood et al.,**  
**2020), mr (triangle symbol and pink line, De Jonge et al., 2014b) and Index1 (yellow circle and line, De Jonge et al., 2014b). On the**  
**right, lateral lines represent calibration errors (RMSE). Finally, the black dashed line corresponds to Canroute's modern MAAT.**  
**The time highlighted in light grey reveals a large fall in tetramethylated brGDGT abundance (6,600–4,700 cal. BP) and a shift in**  
**accumulation rate. The era shown in dark grey highlights the significant decrease in IR (4,700–2,300 cal. BP).**

#### 4.5.2 Regional climate of the northern Mediterranean basin during the last 15,000 years

The Canroute climate reconstruction indicates cold conditions for the Lateglacial and a warming for the Early Holocene (about  
620  $+5 \pm 1^\circ \text{C}$ , Fig. 11a). A similar climatic trend for this period is reconstructed from chironomid data in northern Italy (Fig. 11a),  
with increasing summer temperatures between 14,000 and 10,000 cal. BP of the same order of magnitude (ca.  $+6.5^\circ \text{C}$ ,  
Samartin et al., 2017). The brGDGT signal from Canroute indicates an abrupt warming around 13,500 cal. BP, which is also  
observed in southern Italy from the Lake Matese brGDGT record (Fig. 11a, Robles et al., 2023). The Lateglacial climatic  
changes estimated from the CAN02 sequence are consistent with observations from southern Europe, notably with the  
625 temperature signal of the Lapsou sequence proposed by Duprat-Oualid et al. (2022), located in Cantal (central part of Massif  
Central). The comparison between the pollen signals from Canroute and Lapsou reveals some similarities (e.g., the chronology  
of the Bølling-Allerød between 14,600 and 12,900 cal. BP) and some discrepancies (e.g., the dynamics of Younger Dryas is  
clearly less marked at Canroute). Typical millennial Lateglacial events, such as the Bølling-Allerød and Younger Dryas,  
cannot, however, be seen on both proxies since the brGDGT signal does not reflect such abrupt events (Fig. 11a). The lack of  
630 typical Lateglacial events can be attributed to a low resolution of the record, possibly caused by bioturbation smoothing abrupt  
events (Bradley et al., 2015), a low accumulation rate (Fig. 3a) or a not very marked Lateglacial in the region. Overall, the  
Lateglacial climate signal trend of Canroute fits well with the more regional signal when confronted with different sites and  
proxies of southern Europe.

635 For the Holocene, a spatio-temporal heterogeneity of climate patterns is observed at the northern Mediterranean region scale  
depending on sequences and proxies (Fig. 11). Most of the records indicate, despite a temporal disparity, the presence of a  
Holocene thermal maximum (HTM) between 10,000 and 6,000 cal. BP. Summer and annual temperatures, reconstructed from  
the Swiss Alps, Gulf of Lions, Europe (40–50°N), northern Italy and Massif Central (Heiri et al., 2003; Jalali et al., 2016;  
Samartin et al., 2017; Martin et al., 2020; Herzschuh et al., 2022, Fig. 11b), suggest a HTM between 10,700 and 5,500 cal. BP.  
640 The pollen-based annual temperature reconstruction by Herzschuh et al. (2022) indicates warm conditions for South Europe  
(40–50° N) but not really a HTM (Fig. 11b). When compared to those sequences, only the pollen-based MAT method  
reconstructs a clear HTM between 10,000 and 8,000 cal. BP at Canroute, although less marked in terms of anomalies, and  
probably biased by the high percentages of *Corylus* without modern analogues (Fig. 6).

The BRT method and brGDGT-based reconstructions both indicates a plateau, closer to the annual climate signal proposed by  
645 Herzschuh et al. (2022) for Europe (40–50°N) with the WA-PLS (Fig. 11b). From the Mid-Holocene (ca. 6,000 cal. BP)  
onward, the reconstructions from Canroute indicate a warming trend in agreement with the larger synthesis by Davis et al.  
(2003) and Herzschuh et al. (2022). In contrast, the data from Massif Central (brGDGTs, Martin et al., 2020), Swiss Alps  
(chironomids, Heiri et al., 2003), northern Italy (chironomids, Samartin et al., 2017), and Mediterranean (alkenones, Jalali et  
al., 2016, Fig. 11b) indicate a cooling trend following the HTM. The presence of different patterns in the different  
650 reconstructions can be explained by the type of parameter reconstructed (SST; MTWA, MAAT etc.), by the method used

(local, regional or area-average reconstructions) (Erb et al., 2022), by the proxy itself, but also by local conditions, which can largely influence the proxy record over time. For example, the two reconstructions based on brGDGTs (Fig. 11b) do not indicate the same climate signal. Such difference for the same proxy in the same region (Massif Central) may be due to several factors used to reconstruct the signal: local environment (peatland vs. lake) and altitude (790 vs. 1234 m). On the other side, summer temperature proxies supports the cooling trend that typically follows the HTM (Herzschuh et al., 2022; Heiri et al., 2003; Samartin et al., 2017; Jalali et al., 2016). In the case of the SSTs of the Gulf of Lion proposed by Jalali et al. (2016), the signal is based on alkenones record which could also be biased towards seasonal temperatures (Bader et al., 2020). Additionally, when Canroute's BRT-based signal is compared to the two signals from Herzschuh et al. (2022), i.e., the annual and July signal, only the annual signal appears consistent with Canroute's signal, the seasonal signal indicating a different trend from 8,000 cal. BP onward (Fig. 11b). This supports the hypothesis of the influence of the seasonal (summer) temperatures in the cooling trend following the presence of the HTM in the Mediterranean region in many studies (Wanner et al., 2021). To conclude, in this study, the influence of seasonal temperature in different reconstructions, with independent proxies, is a solid hypothesis to explain the presence of different climatic patterns during the Holocene, particularly for the presence of the Holocene thermic maximum (HTM) in the Mediterranean region.

665

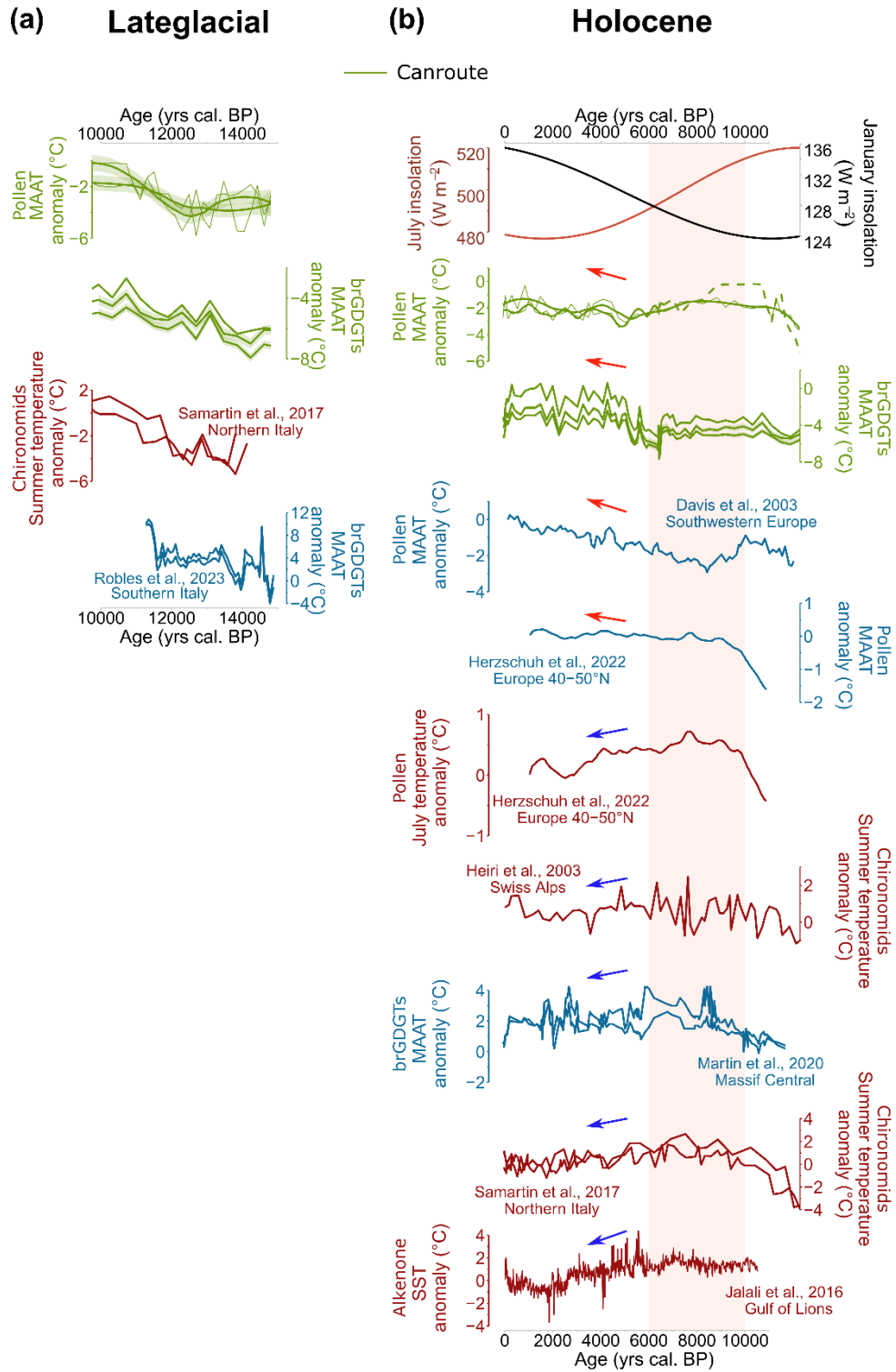


Figure 11: Selected palaeoenvironmental records from southern Europe. (a): Lateglacial climate changes: pollen- and brGDGTs-



based MAATs (Fig. 10); Chironomids-based July temperatures from northern Italy (Samartin et al. 2017); brGDGT-based MAATs from Lake Matese (southern Italy) (Robles et al., 2023). (b): Holocene climate changes: July and January insolation for 44°N (in W m<sup>-2</sup>) (Laskar et al., 2004); MAATs inferred from CAN02 pollen assemblages (the dashed part corresponds to the period where *Corylus* strongly impacts the results obtained with the MAT and over warmed the HTM) and from brGDGTs; MAAT and summer temperature of the European region (40-50°N) from pollen data (Herzschuh et al., 2022); MAATs based on brGDGTs (Martin et al., 2020); Chironomid-based July temperature (Heiri et al., 2003; Samartin et al. 2017); Pollen-based MAAT for south-western Europe (Davis et al., 2003); Sea Surface Temperature (SST) values of the Gulf of Lions (Jalali et al., 2016). The green (Canroute) and blue curves correspond to annual reconstructed temperatures. The red curves correspond to seasonal (summer) reconstructed temperatures. The red box marks the Holocene thermal maximum of the Northern Hemisphere (HTM). Temperature values are expressed as anomalies from the modern climate conditions at each site.

## 5 Conclusion

The palaeoclimatic reconstruction of the last 15,000 years based on the CAN02 sequence has allowed us to compare the southern Massif Central climate changes to the southern Europe one. The Lateglacial and Early Holocene temperature patterns at Canroute are consistent with reconstructions in Italy that show cold conditions during the Lateglacial and a warming for the Early Holocene. The brGDGT and pollen climate signal shows the presence of a Mid-Holocene plateau followed by a Late-Holocene warming instead of a clear mid-Holocene thermal maximum (HTM). The similar trends between the two independent proxies supports the reliability of their respective reconstructions. Our study also highlights the potential causes of the differences between the reconstructions from independent proxies. The influence of local context changes, such as a decrease in water input, on the vegetation and brGDGT records, has been assessed from geochemical, pollen and brGDGT records. The multi-proxy approach points out the importance of investigating changes in the local environmental context for a better interpretation of the reconstructed climate parameters, as those changes could impact pollen and brGDGT records and thus the quality of the reconstructed climate parameters.

Whether for pollen or brGDGTs, the choice of (1) the method, (2) the modern dataset and (3) the calibration is a key step to reconstruct climate parameters and has a significant role in the reliability of reconstructions. Our study corroborates the role of regional calibration in the reliability of reconstructed MAATs. For brGDGTs, a selection of European surface samples from the global peat and soil calibrations could improve the reliability of MAAT reconstructions.

## Appendices

### Appendix A

**Table A1: Location and mean current climate values of sites associated with surface samples for brGDGT analysis. The current climate parameters were extracted with the GIS software QGIS (QGIS.org 2022) from the interpolated database WorldClim2.0 (averaged over the period 1970–2000, Fick and Hijmans, 2017) for annual temperature (MAAT) and precipitation (MAP) data and the CRU TS (version 4.06) measured database (Harris et al., 2020) for monthly temperature and precipitation data (Fig. 1c).**

Peatland	Localization	Sample	Elevation (m)	MAAT (°C)	MAP (mm)
Canroute	43°38'48" N 02°34'35" E	CAN0	790	9.5	895

---

Caroux	43°35'59" N 02°58'25" E	CAR-1-15	1090	9.1	1044
Caroux	43°36'06" N 02°59'01" E	CAR-C2	1090	9.8	1078
Lapsou	45°04'39" N 03°44'44" E	LAP	1200	8.7	697
Lozère	44°27'01" N 03°38'01" E	LOZ	1700	5.5	1534
Nassette	44°28'11" N 03°37'27" E	NAS	1320	5.9	1445
Nassette	44°28'11" N 03°37'27" E	NAS-21	1320	5.9	1445

---

700 **Appendix B**

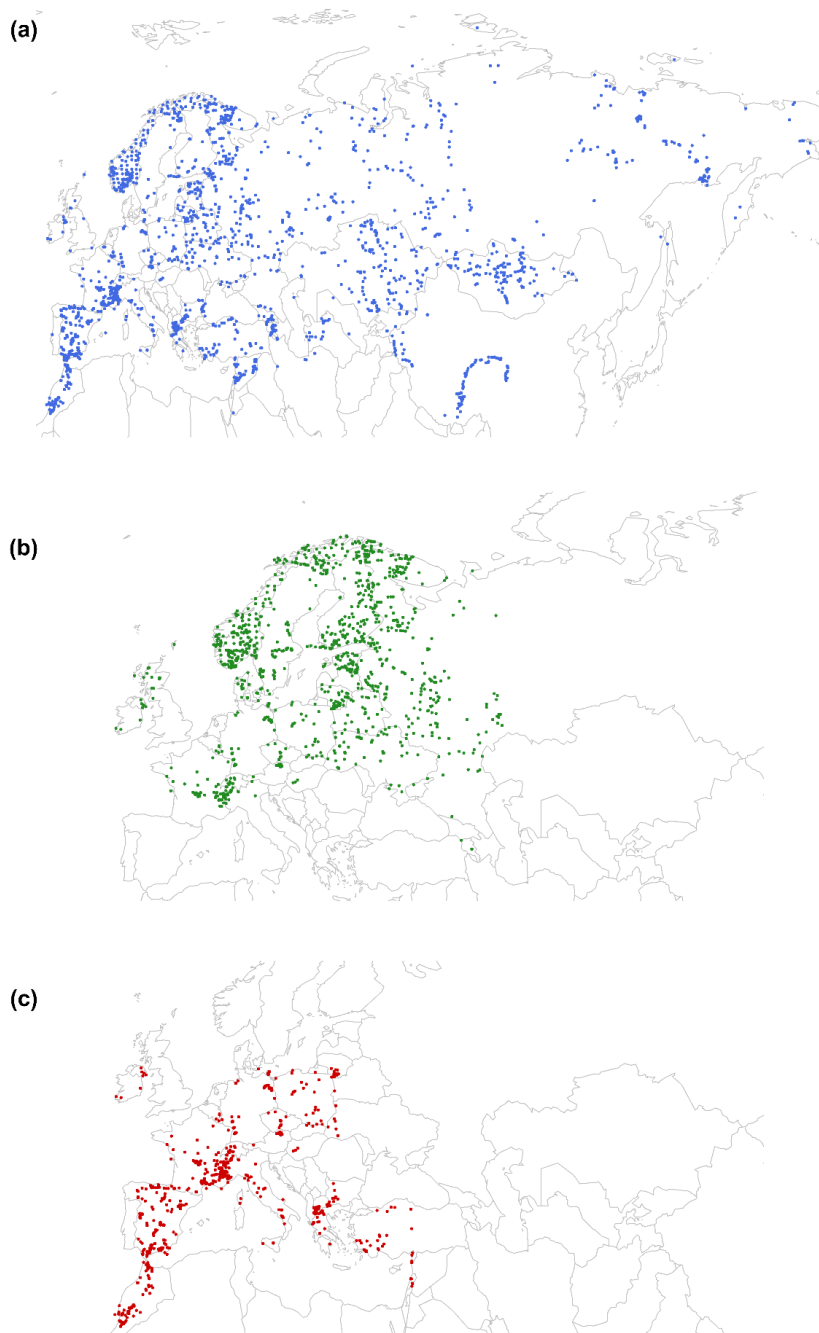
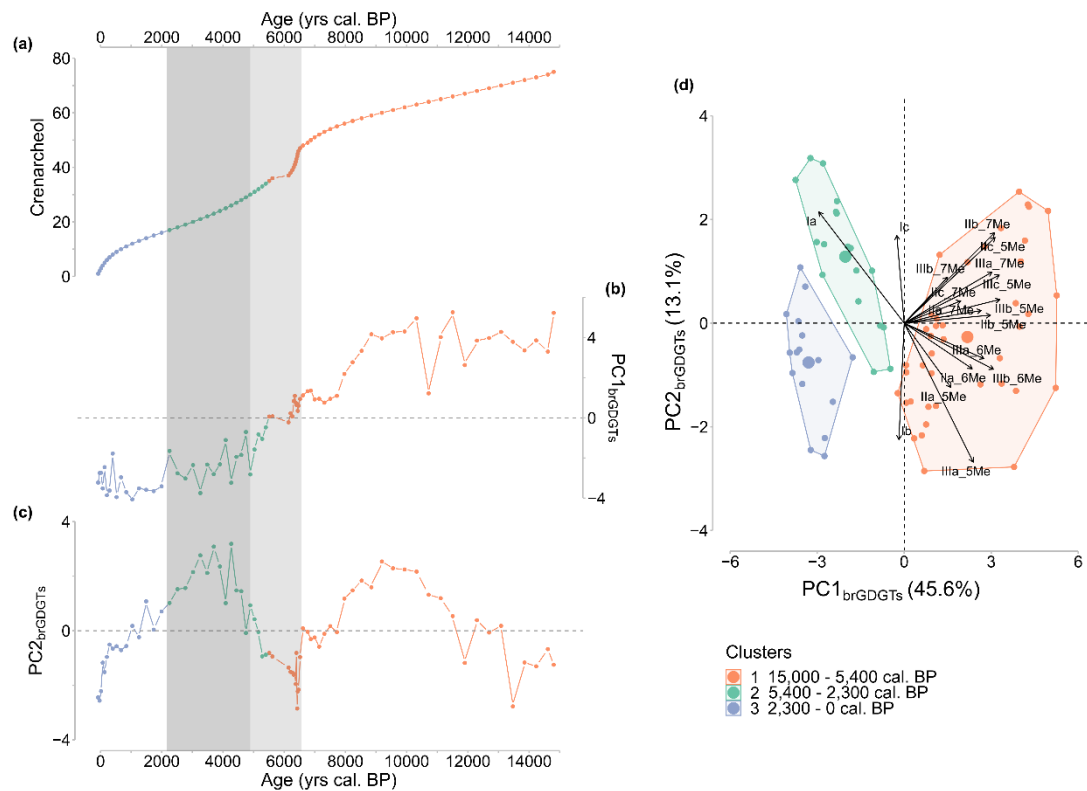


**Figure B1: Location of surface sites used in (a) the Eurasian Pollen Database (EAPDB) compiled by Peyron et al. (2013, 2017); (b) the TEMPCAND (Temperate Europe and Scandinavia) database; (c) the MEDTEMP (Mediterranean and Temperate Europe) database.**

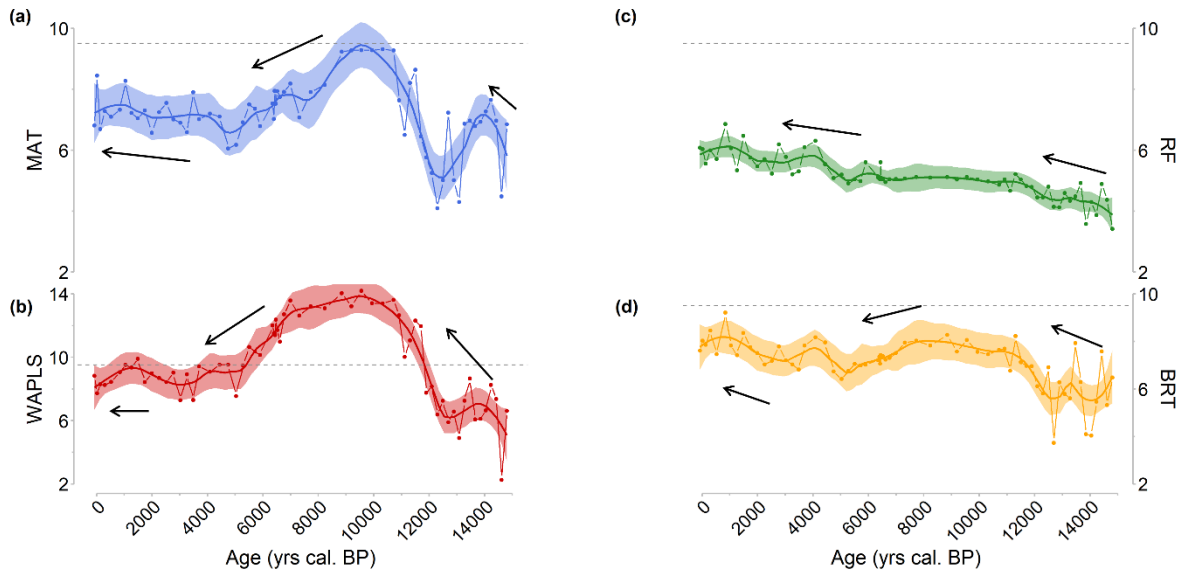
## Appendix C



710

**Figure C1: (a): Crenarcheol. (b): PC1<sub>brGDGTs</sub> of the PCA performed on the brGDGT relative abundances of the Canroute sequence. (c): PC2<sub>brGDGTs</sub> of the PCA performed on the brGDGT relative abundances of the Canroute sequence, (d): PCA results with samples coloured according to the cluster to which they belong.**

## Appendix D



715 **Figure D1: Reconstruction of the mean annual air temperature (MAAT) based on Canroute pollen sequence signal for the four methods used with the TEMPSCAND modern pollen database ((a): MAT, (b): WA-PLS, (c): RF, (d): BRT). The plain line corresponds to locally estimated scatterplot smoothing (loess) regression curves, the shaded area corresponds to the confidence interval used for the model (95 %). The black arrows represent the direction of the climate trends for the different periods considered. Black dashed line: current MAAT at Canroute.**

### Data availability

720 BrGDGTs analysis and pollen-inferred climate reconstruction will be fully available; the pollen counts will be shared thanks to open international databases as EPD, or Neotoma.

### Author contribution

725 Ld performed the analytical work with LD and JA designing R codes. Ld, LD, GM, AE, OP designed the study. LD, GM, AE and OP supervised the study. SDM and LB provided the study material (CAN02 sequence). SDM, CB, LB, SAA and MS contributed to data analysis. AE provided financial support for the project. All authors contributed to the writing of the manuscript.

### Competing interests

The authors declare that they have no conflict of interest.

## Acknowledgements

This study is a part of the DEMETER project supported by the European Research Council (ERC) under the European Union's  
730 Horizon 2020 research and innovation programme (grant agreement No. 852573, PI A. Evin). The sampling of peat cores and  
surface samples was performed during field schools of the University of Montpellier, as part of ORPAM teaching modules.  
The authors thank Frédéric Néri and the CEN Languedoc-Roussillon for fieldwork facilities, ISEM for financial contribution  
to radiocarbon dating, Sandrine Canal for the preparation and treatment of pollen samples, and Jean-Frédéric Terral, Vincent  
Girard and ORPAM students for help with fieldwork and with the preliminary study of the Canroute Peatland. This is ISEM  
735 contribution ISEM 2023-199.

## References

- Ardenghi, N., Mulch, A., Koutsodendris, A., Pross, J., Kahmen, A., and Niedermeyer, E. M.: Temperature and moisture  
variability in the eastern Mediterranean region during Marine Isotope Stages 11–10 based on biomarker analysis of the Tenaghi  
Philippon peat deposit, *Quaternary Science Reviews*, 225, 105977, <https://doi.org/10.1016/j.quascirev.2019.105977>, 2019.
- 740 Ball, D. F.: Loss-on-ignition as an estimate of organic matter and organic carbon in non-calcareous soils, *Journal of Soil  
Science*, 15, 84–92, <https://doi.org/10.1111/j.1365-2389.1964.tb00247.x>, 1964.
- de Beaulieu, J.-L.: Contribution pollenanalytique à l'histoire tardiglaciaire et holocène des Alpes méridionales françaises.  
Doctoral Thesis, Université d'Aix-Marseille III, France, 358 p., 1977.
- de Beaulieu, J.-L., and Reille, M.: Paléoenvironnement tardiglaciaire et holocène des lacs de Pelléautier et Siguret (Hautes-  
745 Alpes, France). I. Histoire de la végétation d'après les analyses polliniques, *Ecologia Mediterranea* 9 (3-4), 19–36, 1983.
- Birks, H. J. B. and Seppä, H.: Pollen-based reconstructions of late-Quaternary climate in Europe – progress, problems, and  
pitfalls, *Acta Palaeobotanica*, 44, 317–334, 2004.
- Birks, H. H. and Birks, H. J. B.: Multi-proxy studies in palaeolimnology, *Veget Hist Archaeobot*, 15, 235–251,  
<https://doi.org/10.1007/s00334-006-0066-6>, 2006.
- 750 Blaauw, M., Christen, J. A., Vázquez, J. E., & Goring, S.: clam: Classical age-depth modelling of cores from deposits, R  
package version 2.5.0, 2(4), 2022.
- Bлага, C. I., Reichert, G.-J., Heiri, O., and Sinninghe Damsté, J. S.: Tetraether membrane lipid distributions in water-column  
particulate matter and sediments: a study of 47 European lakes along a north–south transect, *J Paleolimnol*, 41, 523–540,  
<https://doi.org/10.1007/s10933-008-9242-2>, 2009.
- 755 Breiman, L.: Random Forests, *Machine Learning*, 45, 5–32, <https://doi.org/10.1023/A:1010933404324>, 2001.
- Brewer, S., Guiot, J., Sánchez-Goñi, M. F., and Klotz, S.: The climate in Europe during the Eemian: a multi-method approach  
using pollen data, *Quaternary Science Reviews*, 27, 2303–2315, <https://doi.org/10.1016/j.quascirev.2008.08.029>, 2008.
- Broecker, W. S., Denton, G. H., Edwards, R. L., Cheng, H., Alley, R. B., and Putnam, A. E.: Putting the Younger Dryas cold  
event into context, *Quaternary Science Reviews* 29, 1078–1081, 2010.

- 760 Cartapanis, O., Jonkers, L., Moffa-Sanchez, P., Jaccard, S. L., and de Vernal, A.: Complex spatio-temporal structure of the Holocene thermal maximum, *Nat Commun*, 13, 5662, <https://doi.org/10.1038/s41467-022-33362-1>, 2022.
- Cheddadi, R., Yu, G., Guiot, J., Harrison, S. P., and Prentice, I. C.: The climate of Europe 6000 years ago, *Climate Dynamics*, 13, 1–9, <https://doi.org/10.1007/s003820050148>, 1997.
- Chen, Y., Zheng, F., Yang, H., Yang, W., Wu, R., Liu, X., Liang, H., Chen, H., Pei, H., Zhang, C., Pancost, R. D., and Zeng, Z.: The production of diverse brGDGTs by an Acidobacterium providing a physiological basis for paleoclimate proxies, *Geochimica et Cosmochimica Acta*, 337, 155–165, <https://doi.org/10.1016/j.gca.2022.08.033>, 2022.
- Chevalier, M., Davis, B. A. S., Heiri, O., Seppä, H., Chase, B. M., Gajewski, K., Lacourse, T., Telford, R. J., Finsinger, W., Guiot, J., Kühl, N., Maezumi, S. Y., Tipton, J. R., Carter, V. A., Brussel, T., Phelps, L. N., Dawson, A., Zanon, M., Vallé, F., Nolan, C., Mauri, A., de Vernal, A., Izumi, K., Holmström, L., Marsicek, J., Goring, S., Sommer, P. S., Chaput, M., and Kupriyanov, D.: Pollen-based climate reconstruction techniques for late Quaternary studies, *Earth-Science Reviews*, 210, 33, 770 2020.
- Davies, S. J., Lamb, H. F., and Roberts, S. J.: Micro-XRF Core Scanning in Palaeolimnology: Recent Developments, in: *Micro-XRF Studies of Sediment Cores: Applications of a non-destructive tool for the environmental sciences*, edited by: Croudace, I. W. and Rothwell, R. G., Springer Netherlands, Dordrecht, 189–226, [https://doi.org/10.1007/978-94-017-9849-5\\_7](https://doi.org/10.1007/978-94-017-9849-5_7), 2015.
- 775 Davis, B. A. S., Brewer, S., Stevenson, A. C., and Guiot, J.: The temperature of Europe during the Holocene reconstructed from pollen data, *Quaternary Science Reviews*, 22, 1701–1716, [https://doi.org/10.1016/S0277-3791\(03\)00173-2](https://doi.org/10.1016/S0277-3791(03)00173-2), 2003.
- Davtian, N., Bard, E., Darfeuille, S., Ménot, G., and Rostek, F.: The Novel Hydroxylated Tetraether Index RI-OH' as a Sea Surface Temperature Proxy for the 160–45 ka BP Period Off the Iberian Margin, *Palaeoceanography and Palaeoclimatology*, 36, e2020PA004077, <https://doi.org/10.1029/2020PA004077>, 2021.
- 780 De Jonge, C., Kuramae, E. E., Radujković, D., Weedon, J. T., Janssens, I. A., and Peterse, F.: The influence of soil chemistry on branched tetraether lipids in mid- and high latitude soils: Implications for brGDGT- based palaeothermometry, *Geochimica et Cosmochimica Acta*, 310, 95–112, <https://doi.org/10.1016/j.gca.2021.06.037>, 2021.
- De Jonge, C., Stadnitskaia, A., Hopmans, E. C., Cherkashov, G., Fedotov, A., and Sinninghe Damsté, J. S.: In situ produced branched glycerol dialkyl glycerol tetraethers in suspended particulate matter from the Yenisei River, Eastern Siberia, *Geochimica et Cosmochimica Acta*, 125, 476–491, <https://doi.org/10.1016/j.gca.2013.10.031>, 2014a.
- 785 De Jonge, C., Hopmans, E. C., Zell, C. I., Kim, J.-H., Schouten, S., and Sinninghe Damsté, J. S.: Occurrence and abundance of 6-methyl branched glycerol dialkyl glycerol tetraethers in soils: Implications for palaeoclimate reconstruction, *Geochimica et Cosmochimica Acta*, 141, 97–112, <https://doi.org/10.1016/j.gca.2014.06.013>, 2014b.
- De Jonge, C., Radujković, D., Sigurdsson, B. D., Weedon, J. T., Janssens, I., and Peterse, F.: Lipid biomarker temperature proxy responds to abrupt shift in the bacterial community composition in geothermally heated soils, *Organic Geochemistry*, 137, 103897, <https://doi.org/10.1016/j.orggeochem.2019.07.0006>, 2019.
- 790

- Dearing Crampton-Flood, E., Tierney, J. E., Peterse, F., Kirkels, F. M. S. A., and Sinninghe Damsté, J. S.: BayMBT: A Bayesian calibration model for branched glycerol dialkyl glycerol tetraethers in soils and peats, *Geochimica et Cosmochimica Acta*, 268, 142–159, <https://doi.org/10.1016/j.gca.2019.09.043>, 2020.
- 795 De'Ath, G.: Boosted Trees for Ecological. Modelling and Prediction, *Ecology*, 88, 243–251, [https://doi.org/10.1890/0012-9658\(2007\)88\[243:BTFEMA\]2.0.CO;2](https://doi.org/10.1890/0012-9658(2007)88[243:BTFEMA]2.0.CO;2), 2007.
- Decorsiere, J., Delamare-Deboutteville, J. and Lecerf, C.: Reconstitution de 13 500 ans d'histoire d'une tourbière dans le Sud de la France. *Orpalm Synthesis*, 12, 29–39, 2019.
- Denton, G. H., Anderson, R. F., Toggweiler, J. R., Edwards, R. L., Schaefer, J. M., and Putnam, A. E.: The Last Glacial  
800 Termination, *Science* 328, 1652–1656, 2010.
- Ding, S., Schwab, V. F., Ueberschaar, N., Roth, V.-N., Lange, M., Xu, Y., Gleixner, G., and Pohnert, G.: Identification of novel 7-methyl and cyclopentanyl branched glycerol dialkyl glycerol tetraethers in lake sediments, *Organic Geochemistry*, 102, 52–58, <https://doi.org/10.1016/j.orggeochem.2016.09.009>, 2016.
- Dugerdil, L., Joannin, S., Peyron, O., Jouffroy-Bapicot, I., Vannièrè, B., Boldgiv, B., Unkelbach, J., Behling, H., and Ménot,  
805 G.: Climate reconstructions based on GDGT and pollen surface databases from Mongolia and Baikal area: calibrations and applicability to extremely cold–dry environments over the Late Holocene, *Clim. Past*, 17, 1199–1226, <https://doi.org/10.5194/cp-17-1199-2021,2021a>.
- Dugerdil, L., Ménot, G., Peyron, O., Jouffroy-Bapicot, I., Ansanay-Alex, S., Antheaume, I., Behling, H., Boldgiv, B., Develle, A.-L., Grossi, V., Magail, J., Makou, M., Robles, M., Unkelbach, J., Vannièrè, B., and Joannin, S.: Late Holocene Mongolian  
810 climate and environment reconstructions from brGDGTs, NPPs and pollen transfer functions for Lake Ayrag: Palaeoclimate implications for Arid Central Asia, *Quaternary Science Reviews*, 273, 107235, <https://doi.org/10.1016/j.quascirev.2021.107235>, 2021b.
- Duprat-Oualid, F., Bégeot, C., Peyron, O., Rius, D., Millet, L., and Magny, M.: High-frequency vegetation and climatic changes during the Lateglacial inferred from the Lapsou pollen record (Cantal, southern Massif Central, France), *Quaternary  
815 International*, 636, 69–80, <https://doi.org/10.1016/j.quaint.2022.04.012>, 2022.
- Elith, J., Leathwick, J. R., and Hastie, T.: A working guide to boosted regression trees, *Journal of Animal Ecology*, 77, 802–813, <https://doi.org/10.1111/j.1365-2656.2008.01390.x>, 2008.
- Erb, M. P., McKay, N. P., Steiger, N., Dee, S., Hancock, C., Ivanovic, R. F., Gregoire, L. J., and Valdes, P.: Reconstructing Holocene temperatures in time and space using palaeoclimate data assimilation, *Clim. Past*, 18, 2599–2629,  
820 <https://doi.org/10.5194/cp-18-2599-2022>, 2022.
- Fick, S. E. and Hijmans, R. J.: WorldClim 2: new 1-km spatial resolution climate surfaces for global land areas, *International Journal of Climatology*, 37, 4302–4315, <https://doi.org/10.1002/joc.5086>, 2017.
- Grimm, E. C.: CONISS: a FORTRAN 77 program for stratigraphically constrained cluster analysis by the method of incremental sum of squares, *Computers & Geosciences*, 13, 13–35, [https://doi.org/10.1016/0098-3004\(87\)90022-7](https://doi.org/10.1016/0098-3004(87)90022-7), 1987.



- 825 Guiot, J.: Methodology of the last climatic cycle reconstruction in France from pollen data, *Palaeogeography, Palaeoclimatology, Palaeoecology*, 80, 49–69, [https://doi.org/10.1016/0031-0182\(90\)90033-4](https://doi.org/10.1016/0031-0182(90)90033-4), 1990.
- Halamka, T. A., Raberg, J. H., McFarlin, J. M., Younkin, A. D., Mulligan, C., Liu, X., and Kopf, S. H.: Production of diverse brGDGTs by *Acidobacterium Solibacter usitatus* in response to temperature, pH, and O<sub>2</sub> provides a culturing perspective on br GDGT proxies and biosynthesis, *Geobiology*, 21, 102–118, <https://doi.org/10.1111/gbi.12525>, 2023.
- 830 Harris, I., Osborn, T. J., Jones, P., and Lister, D.: Version 4 of the CRU TS monthly high-resolution gridded multivariate climate database, *Sci Data*, 7, 109, <https://doi.org/10.1038/s41597-020-0453-3>, 2020.
- Heiri, O., Lotter, A. F., Hausmann, S., and Kienast, F.: A chironomid-based Holocene summer air temperature reconstruction from the Swiss Alps, *The Holocene*, 13, 477–484, <https://doi.org/10.1191/0959683603hl640ft>, 2003.
- Herzschuh, U., Böhmer, T., Chevalier, M., Dallmeyer, A., Li, C., Cao, X., Hébert, R., Peyron, O., Nazarova, L., Novenko, E.
- 835 Y., Park, J., Rudaya, N. A., Schlütz, F., Shumilovskikh, L. S., Tarasov, P. E., Wang, Y., Wen, R., Xu, Q., and Zheng, Z.: Regional pollen-based Holocene temperature and precipitation patterns depart from the Northern Hemisphere mean trends, *Atmospheric Dynamics/Terrestrial Archives/Holocene*, <https://doi.org/10.5194/egusphere-2022-127>, 2022.
- Hijmans, R. J., Phillips, S., Leathwick, J., Elith, J.: Package “dismo”, *Circles*, 9, 1-68, 2017.
- Hopmans, E. C., Weijers, J. W. H., Schefuß, E., Herfort, L., Sinninghe Damsté, J. S., and Schouten, S.: A novel proxy for
- 840 terrestrial organic matter in sediments based on branched and isoprenoid tetraether lipids, *Earth and Planetary Science Letters*, 224, 107–116, <https://doi.org/10.1016/j.epsl.2004.05.012>, 2004.
- Hopmans, E. C., Schouten, S., and Sinninghe Damsté, J. S.: The effect of improved chromatography on GDGT-based palaeoproxies, *Organic Geochemistry*, 93, 1–6, <https://doi.org/10.1016/j.orggeochem.2015.12.006>, 2016.
- Huguet, A., Fosse, C., Laggoun-Défarge, F., Toussaint, M.-L., and Derenne, S.: Occurrence and distribution of glycerol dialkyl
- 845 glycerol tetraethers in a French peat bog, *Organic Geochemistry*, 41, 559–572, <https://doi.org/10.1016/j.orggeochem.2010.02.015>, 2010.
- Huguet, C., Hopmans, E. C., Febo-Ayala, W., Thompson, D. H., Sinninghe Damsté, J. S., and Schouten, S.: An improved method to determine the absolute abundance of glycerol dibiphytanyl glycerol tetraether lipids, *Organic Geochemistry*, 37, 1036–1041, <https://doi.org/10.1016/j.orggeochem.2006.05.008>, 2006.
- 850 Jalali, B., Sicre, M.-A., Bassetti, M.-A., and Kallel, N.: Holocene climate variability in the North-Western Mediterranean Sea (Gulf of Lions), *Clim. Past*, 12, 91–101, <https://doi.org/10.5194/cp-12-91-2016>, 2016.
- Joosten, H.: Current soil carbon loss and land degradation globally: where are the hotspots and why there?, *Soil carbon: science, management and policy for multiple benefits*, 224–234, <https://doi.org/10.1079/9781780645322.0224>, 2015.
- Josse, J. and Husson, F.: missMDA: A Package for Handling Missing Values in Multivariate Data Analysis, *Journal of*
- 855 *Statistical Software*, 70, 1-31, <https://doi.org/10.18637/jss.v070.i01>, 2016.
- Juggins, S. and Juggins, M. S.: Package ‘rioja’. An R Package for the Analysis of Quaternary Science Data., 0.9, 26, 2020.
- Kassambara, A., and Mundt, F.: Factoextra: extract and visualize the results of multivariate data analyses, *R package version*, 1, 337-354, 2017.

- 860 Kaufman, D., McKay, N., Routson, C., Erb, M., Dätwyler, C., Sommer, P. S., Heiri, O., and Davis, B.: Holocene global mean surface temperature, a multi-method reconstruction approach, *Sci Data*, 7, 201, <https://doi.org/10.1038/s41597-020-0530-7>, 2020.
- Laskar, J., Robutel, P., Joutel, F., Gastineau, M., Correia, A. C. M., and Levrard, B.: A long-term numerical solution for the insolation quantities of the Earth, *A&A*, 428, 261–285, <https://doi.org/10.1051/0004-6361:20041335>, 2004.
- 865 Le, S., Josse, J., and Husson, F.: FactoMineR: An R Package for Multivariate Analysis, *Journal of Statistical Software*, 25(1), 1–18, <https://www.jstatsoft.org/v25/i01/>, 2008.
- Le Houérou, H.-N.: Biogeography of the arid steppeland north of the Sahara, *Journal of Arid Environments*, 48, 103–128, 2001.
- Li, J., Pancost, R. D., Naafs, B. D. A., Yang, H., Zhao, C., and Xie, S.: Distribution of glycerol dialkyl glycerol tetraether (GDGT) lipids in a hypersaline lake system, *Organic Geochemistry*, 99, 113–124, <https://doi.org/10.1016/j.orggeochem.2016.06.007>, 2016.
- 870 Liu, Z., Zhu, J., Rosenthal, Y., Zhang, X., Otto-Bliesner, B. L., Timmermann, A., Smith, R. S., Lohmann, G., Zheng, W., and Elison Timm, O.: The Holocene temperature conundrum, *Proc. Natl. Acad. Sci. U.S.A.*, 111, <https://doi.org/10.1073/pnas.1407229111>, 2014.
- Marcott, S. A., Shakun, J. D., Clark, P. U., and Mix, A. C.: A Reconstruction of Regional and Global Temperature for the Past 11,300 Years, *Science*, 339, 1198–1201, <https://doi.org/10.1126/science.1228026>, 2013.
- 875 Marriner, N., Kaniewski, D., Pourkerman, M., and Devillers, B.: Anthropocene tipping point reverses long-term Holocene cooling of the Mediterranean Sea: A meta-analysis of the basin’s Sea Surface Temperature records, *Earth-Science Reviews*, 227, 103986, <https://doi.org/10.1016/j.earscirev.2022.103986>, 2022.
- Marsicek, J., Shuman, B. N., Bartlein, P. J., Shafer, S. L., and Brewer, S.: Reconciling divergent trends and millennial variations in Holocene temperatures, *Nature*, 554, 19, <https://doi.org/doi:10.1038/nature25464>, 2018.
- 880 Martin, C., Ménot, G., Thouveny, N., Davtian, N., Andrieu-Ponel, V., Reille, M., and Bard, E.: Impact of human activities and vegetation changes on the tetraether sources in Lake St Front (Massif Central, France), *Organic Geochemistry*, 135, 38–52, <https://doi.org/10.1016/j.orggeochem.2019.06.005>, 2019.
- Martin, C., Ménot, G., Thouveny, N., Peyron, O., Andrieu-Ponel, V., Montade, V., Davtian, N., Reille, M., and Bard, E.: Early Holocene thermal maximum recorded by branched tetraethers and pollen in Western Europe (Massif Central, France), *Quaternary Science Reviews*, 228, 106109, <https://doi.org/10.1016/j.quascirev.2019.106109>, 2020.
- 885 Martínez-Sosa, P., Tierney, J. E., Stefanescu, I. C., Dearing Crampton-Flood, E., Shuman, B. N., and Routson, C.: A global Bayesian temperature calibration for lacustrine brGDGTs, *Geochimica et Cosmochimica Acta*, 305, 87–105, <https://doi.org/10.1016/j.gca.2021.04.038>, 2021.
- 890 Mauri, A., Davis, B. A. S., Collins, P. M., and Kaplan, J. O.: The influence of atmospheric circulation on the mid-Holocene climate of Europe: a data–model comparison, *Clim. Past*, 10, 1925–1938, <https://doi.org/10.5194/cp-10-1925-2014>, 2014.

- Mauri, A., Davis, B. A. S., Collins, P. M., and Kaplan, J. O.: The climate of Europe during the Holocene: a gridded pollen-based reconstruction and its multi-proxy evaluation, *Quaternary Science Reviews*, 112, 109–127, <https://doi.org/10.1016/j.quascirev.2015.01.013>, 2015.
- 895 Mayewski, P. A., Rohling, E. E., Curt Stager, J., Karlén, W., Maasch, K. A., Meecker, L. D., Meyerson, E. A., Gasse, F., van Kreveland, S., Holmgren, K., Lee-Thorp, J., Rosqvist, G., Rack, F., Staubwasser, M., Schneider, R. R., and Steig, E. J.: Holocene climate variability, *Quat. res.*, 62, 243–255, <https://doi.org/10.1016/j.yqres.2004.07.001>, 2004.
- Miras, Y., Vergne, V., Guenet, P., and Surmely, F.: Le Massif Central : premières traces d’anthropisation révélées par l’analyse pollinique des zones humides corrélées aux données archéologiques. In: Richard, H. (Dir.), *Néolithisation précoce. Premières*  
900 *traces d’anthropisation du couvert végétal à partir des données polliniques*. Presses Universitaires Franc-Comtoises, Besançon, pp. 89–105, 2004.
- Mohammad, A. G. and Adam, M. A.: The impact of vegetative cover type on runoff and soil erosion under different land uses, *CATENA*, 81, 97–103, <https://doi.org/10.1016/j.catena.2010.01.008>, 2010.
- Moore, P.D.: The ecology of peat-forming processes: a review, *International Journal of Coal Geology*, 12(1-4), 89-103, 1989.
- 905 Muller, S.D., Brémond, L., Girard, V., Terral, J.-F.: Végétation de la tourbière de Canroute, dans les Monts de Lacaune (Le Margnès, Tarn), *Orpalm Synthesis*, 11(1), 9-13, 2018.
- Naafs, B. D. A., Inglis, G. N., Zheng, Y., Amesbury, M. J., Biester, H., Bindler, R., Blewett, J., Burrows, M. A., Del Castillo Torres, D., Chambers, F. M., Cohen, A. D., Evershed, R. P., Feakins, S. J., Gałka, M., Gallego-Sala, A., Gandois, L., Gray, D. M., Hatcher, P. G., Honorio Coronado, E. N., Hughes, P. D. M., Hugué, A., Könönen, M., Laggoun-Défarge, F., Lähteenoja,  
910 O., Lamentowicz, M., Marchant, R., McClymont, E., Pontevedra-Pombal, X., Ponton, C., Pourmand, A., Rizzuti, A. M., Rochefort, L., Schellekens, J., De Vleeschouwer, F., and Pancost, R. D.: Introducing global peat-specific temperature and pH calibrations based on brGDGT bacterial lipids, *Geochimica et Cosmochimica Acta*, 208, 285–301, <https://doi.org/10.1016/j.gca.2017.01.038>, 2017a.
- Naafs, B. D. A., Gallego-Sala, A. V., Inglis, G. N., and Pancost, R. D.: Refining the global branched glycerol dialkyl glycerol  
915 tetraether (brGDGT) soil temperature calibration, *Organic Geochemistry*, 106, 48–56, <https://doi.org/10.1016/j.orggeochem.2017.01.009>, 2017b.
- Naafs, B. D. A., Inglis, G. N., Blewett, J., McClymont, E. L., Lauretano, V., Xie, S., Evershed, R. P., and Pancost, R. D.: The potential of biomarker proxies to trace climate, vegetation, and biogeochemical processes in peat: A review, *Global and Planetary Change*, 179, 57–79, <https://doi.org/10.1016/j.gloplacha.2019.05.006>, 2019.
- 920 Naafs, B. D. A., Oliveira, A. S. F., and Mulholland, A. J.: Molecular dynamics simulations support the hypothesis that the brGDGT paleothermometer is based on homeoviscous adaptation, *Geochimica et Cosmochimica Acta*, 312, 44–56, <https://doi.org/10.1016/j.gca.2021.07.034>, 2021.
- NASA JPL.: NASA Shuttle Radar Topography Mission Global 1 arc second [Data set], NASA EOSDIS Land Processes DAAC, 2013

- 925 Pearson, A. and Ingalls, A. E.: Assessing the Use of Archaeal Lipids as Marine Environmental Proxies, *Annual Review of Earth and Planetary Sciences*, 41, 359–384, <https://doi.org/10.1146/annurev-earth-050212-123947>, 2013.
- Pearson, E. J., Juggins, S., Talbot, H. M., Weckström, J., Rosén, P., Ryves, D. B., Roberts, S. J., and Schmidt, R.: A lacustrine GDGT-temperature calibration from the Scandinavian Arctic to Antarctic: Renewed potential for the application of GDGT-palaeothermometry in lakes, *Geochimica et Cosmochimica Acta*, 75, 6225–6238, <https://doi.org/10.1016/j.gca.2011.07.042>,  
930 2011.
- Peterse, F., van der Meer, J., Schouten, S., Weijers, J. W. H., Fierer, N., Jackson, R. B., Kim, J.-H., and Sinninghe Damsté, J. S.: Revised calibration of the MBT–CBT palaeotemperature proxy based on branched tetraether membrane lipids in surface soils, *Geochimica et Cosmochimica Acta*, 96, 215–229, <https://doi.org/10.1016/j.gca.2012.08.011>, 2012.
- Peyron, O., Bégeot, C., Brewer, S., Heiri, O., Magny, M., Millet, L., Ruffaldi, P., Van Campo, E., and Yu, G.: Late-Glacial  
935 climatic changes in Eastern France (Lake Lautrey) from pollen, lake-levels, and chironomids, *Quat. res.*, 64, 197–211, <https://doi.org/10.1016/j.yqres.2005.01.006>, 2005.
- Peyron, O., Magny, M., Goring, S., Joannin, S., de Beaulieu, J.-L., Brugiapaglia, E., Sadori, L., Garfi, G., Kouli, K., Ioakim, C., and Combourieu-Nebout, N.: Contrasting patterns of climatic changes during the Holocene across the Italian Peninsula reconstructed from pollen data, *Clim. Past*, 9, 1233–1252, <https://doi.org/10.5194/cp-9-1233-2013>, 2013.
- 940 Peyron, O., Combourieu-Nebout, N., Brayshaw, D., Goring, S., Andrieu-Ponel, V., Desprat, S., Fletcher, W., Gambin, B., Ioakim, C., Joannin, S., Kotthoff, U., Kouli, K., Montade, V., Pross, J., Sadori, L., and Magny, M.: Precipitation changes in the Mediterranean basin during the Holocene from terrestrial and marine pollen records: a model-data comparison, *Clim. Past*, 13, 249–265, <https://doi.org/10.5194/cp-13-249-2017>, 2017.
- Peyron, O., Goring, S., Dormoy, I., Kotthoff, U., Pross, J., de Beaulieu, J.-L., Drescher-Schneider, R., Vannièrè, B., and  
945 Magny, M.: Holocene seasonality changes in the central Mediterranean region reconstructed from the pollen sequences of Lake Accesa (Italy) and Tenaghi Philippon (Greece), *The Holocene*, 21, 131–146, <https://doi.org/10.1177/0959683610384162>, 2011.
- Ponel, P., Guiter, F., Gandouin, E., Peyron, O., and de Beaulieu, J.-L.: Late-Glacial palaeotemperatures and palaeoprecipitations in the Aubrac Mountains (French Massif Central) reconstructed from multiproxy analyses (Coleoptera,  
950 chironomids and pollen), *Quaternary International*, <https://doi.org/10.1016/j.quaint.2022.02.005>, 2022.
- Prasad, A. M., Iverson, L. R., and Liaw, A.: Newer Classification and Regression Tree Techniques: Bagging and Random Forests for Ecological Prediction, *Ecosystems*, 9, 181–199, <https://doi.org/10.1007/s10021-005-0054-1>, 2006.
- QGIS.org.: QGIS Geographic Information System. QGIS Association, <https://www.qgis.org/>, 2022.
- R Core Team: R: A language and environment for statistical computing, R Foundation for Statistical Computing, Vienna,  
955 Austria, <https://www.R-project.org>, 2022.
- Raberg, J. H., Harning, D. J., Crump, S. E., de Wet, G., Blumm, A., Kopf, S., Geirsdóttir, Á., Miller, G. H., and Sepúlveda, J.: Revised fractional abundances and warm-season temperatures substantially improve brGDGT calibrations in lake sediments, *Biogeosciences*, 18, 3579–3603, <https://doi.org/10.5194/bg-18-3579-2021>, 2021. Raberg, J. H., Miller, G. H., Geirsdóttir, Á.,

- and Sepúlveda, J.: Near-universal trends in brGDGT lipid distributions in nature, *Sci. Adv.*, 8, eabm7625, 960 <https://doi.org/10.1126/sciadv.abm7625>, 2022.
- Ramos-Román, M. J., De Jonge, C., Magyari, E., Veres, D., Ilvonen, L., Develle, A.-L., and Seppä, H.: Lipid biomarker (brGDGT)- and pollen-based reconstruction of temperature change during the Middle to Late Holocene transition in the Carpathians, *Global and Planetary Change*, 215, 103859, <https://doi.org/10.1016/j.gloplacha.2022.103859>, 2022.
- Rao, Z., Guo, H., Wei, S., Cao, J., and Jia, G.: Influence of water conditions on peat brGDGTs: A modern investigation and 965 its palaeoclimatic implications, *Chemical Geology*, 606, 120993, <https://doi.org/10.1016/j.chemgeo.2022.120993>, 2022.
- Reimer, P. J., Austin, W. E. N., Bard, E., Bayliss, A., Blackwell, P. G., Bronk Ramsey, C., Butzin, M., Cheng, H., Edwards, R. L., Friedrich, M., Grootes, P. M., Guilderson, T. P., Hajdas, I., Heaton, T. J., Hogg, A. G., Hughen, K. A., Kromer, B., Manning, S. W., Muscheler, R., Palmer, J. G., Pearson, C., van der Plicht, J., Reimer, R. W., Richards, D. A., Scott, E. M., Southon, J. R., Turney, C. S. M., Wacker, L., Adolphi, F., Büntgen, U., Capano, M., Fahrni, S. M., Fogtmann-Schulz, A., 970 Friedrich, R., Köhler, P., Kudsk, S., Miyake, F., Olsen, J., Reinig, F., Sakamoto, M., Sookdeo, A., and Talamo, S.: The IntCal20 Northern Hemisphere Radiocarbon Age Calibration Curve (0–55 cal kBP), *Radiocarbon*, 62, 725–757, <https://doi.org/10.1017/RDC.2020.41>, 2020.
- Renssen, H., Seppä, H., Crosta, X., Goosse, H., and Roche, D. M.: Global characterization of the Holocene thermal maximum, *Quaternary Science Reviews*, 48, 7–19, <https://doi.org/10.1016/j.quascirev.2012.05.022>, 2012.
- 975 Robles, M., Peyron, O., Brugiapaglia, E., Ménot, G., Dugerdil, L., Ollivier, V., Ansanay-Alex, S., Develle, A.-L., Tozalakyan, P., Meliksetian, K., Sahakyan, K., Sahakyan, L., Perello, B., Badalyan, R., Colombié, C., and Joannin, S.: Impact of climate changes on vegetation and human societies during the Holocene in the South Caucasus (Vanevan, Armenia): A multiproxy approach including pollen, NPPs and brGDGTs, *Quaternary Science Reviews*, 277, 107297, <https://doi.org/10.1016/j.quascirev.2021.107297>, 2022.
- 980 Robles, M., Peyron, O., Ménot, G., Brugiapaglia, E., Wulf, S., Appelt, O., Blache, M., Vannière, B., Dugerdil, L., Paura, B., Ansanay-Alex, S., Cromartie, A., Charlet, L., Guédron, S., de Beaulieu, J.-L., and Joannin, S.: Climate changes during the Lateglacial in South Europe: new insights based on pollen and brGDGTs of Lake Matese in Italy, *Continental Surface Processes/Terrestrial Archives/Pleistocene*, <https://doi.org/10.5194/cp-2022-54>, 2023.
- Rodrigo-Gámiz, M., García-Alix, A., Jiménez-Moreno, G., Ramos-Román, M. J., Camuera, J., Toney, J. L., Sachse, D., 985 Anderson, R. S., and Sinninghe Damsté, J. S.: Palaeoclimate reconstruction of the last 36 kyr based on branched glycerol dialkyl glycerol tetraethers in the Padul palaeolake record (Sierra Nevada, southern Iberian Peninsula), *Quaternary Science Reviews*, 281, 107434, <https://doi.org/10.1016/j.quascirev.2022.107434>, 2022.
- Russell, J. M., Hopmans, E. C., Loomis, S. E., Liang, J., and Sinninghe Damsté, J. S.: Distributions of 5- and 6-methyl branched glycerol dialkyl glycerol tetraethers (brGDGTs) in East African lake sediment: Effects of temperature, pH, and new lacustrine 990 palaeotemperature calibrations, *Organic Geochemistry*, 117, 56–69, <https://doi.org/10.1016/j.orggeochem.2017.12.003>, 2018.
- RStudio Team.: RStudio: Integrated Development for R, RStudio, PBC, Boston, MA [burl](https://www.rstudio.com/), 2020.

- Sahonero-Canavesi, D. X., Siliakus, M. F., Abdala Asbun, A., Koenen, M., Von Meijenfeldt, F. A. B., Boeren, S., Bale, N. J., Engelman, J. C., Fiege, K., Strack Van Schijndel, L., Sinninghe Damsté, J. S., and Villanueva, L.: Disentangling the lipid divide: Identification of key enzymes for the biosynthesis of membrane-spanning and ether lipids in Bacteria, *Sci. Adv.*, 8, eabq8652, <https://doi.org/10.1126/sciadv.abq8652>, 2022.
- Salonen, J. S., Korpela, M., Williams, J. W., and Luoto, M.: Machine-learning based reconstructions of primary and secondary climate variables from North American and European fossil pollen data, *Sci Rep*, 9, 15805, <https://doi.org/10.1038/s41598-019-52293-4>, 2019.
- Samartin, S., Heiri, O., Joos, F., Renssen, H., Franke, J., Brönnimann, S., and Tinner, W.: Warm Mediterranean mid-Holocene summers inferred from fossil midge assemblages, *Nature Geosci*, 10, 207–212, <https://doi.org/10.1038/ngeo2891>, 2017.
- Schouten, S., Hopmans, E. C., and Sinninghe Damsté, J. S.: The organic geochemistry of glycerol dialkyl glycerol tetraether lipids: A review, *Organic Geochemistry*, 54, 19–61, <https://doi.org/10.1016/j.orggeochem.2012.09.006>, 2013.
- Schouten, S., Hopmans, E. C., Pancost, R. D., and Damsté, J. S. S.: Widespread occurrence of structurally diverse tetraether membrane lipids: Evidence for the ubiquitous presence of low-temperature relatives of hyperthermophiles, *Proceedings of the National Academy of Sciences*, 97, 14421–14426, <https://doi.org/10.1073/pnas.97.26.14421>, 2000.
- Schouten, S., Rijpstra, W. I. C., Durisch-Kaiser, E., Schubert, C. J., and Sinninghe Damsté, J. S.: Distribution of glycerol dialkyl glycerol tetraether lipids in the water column of Lake Tanganyika, *Organic Geochemistry*, 53, 34–37, <https://doi.org/10.1016/j.orggeochem.2012.01.009>, 2012.
- Seppä, H. and Bennett, K. D.: Quaternary pollen analysis: recent progress in palaeoecology and palaeoclimatology, *Progress in Physical Geography*, 27, 548–579, 2003.
- Silva-Sánchez, N., Martínez Cortizas, A., and López-Merino, L.: Linking forest cover, soil erosion and mire hydrology to late-Holocene human activity and climate in NW Spain, *The Holocene*, 24, 714–725, <https://doi.org/10.1177/0959683614526934>, 2014.
- Sinninghe Damsté, J. S.: Spatial heterogeneity of sources of branched tetraethers in shelf systems: The geochemistry of tetraethers in the Berau River delta (Kalimantan, Indonesia), *Geochimica et Cosmochimica Acta*, 186, 13–31, <https://doi.org/10.1016/j.gca.2016.04.033>, 2016.
- Smith, A. C., Wynn, P. M., Barker, P. A., Leng, M. J., Noble, S. R., and Tych, W.: North Atlantic forcing of moisture delivery to Europe throughout the Holocene, *Sci Rep*, 6, 24745, <https://doi.org/10.1038/srep24745>, 2016.
- Sugita, S., Parshall, T., Calcote, R.: Detecting differences in vegetation among paired sites using pollen records, *The Holocene*, 16, 1123–1135, 2006.
- Sun, Q., Chu, G., Liu, M., Xie, M., Li, S., Ling, Y., Wang, X., Shi, L., Jia, G., and Lü, H.: Distributions and temperature dependence of branched glycerol dialkyl glycerol tetraethers in recent lacustrine sediments from China and Nepal, *Journal of Geophysical Research: Biogeosciences*, 116, <https://doi.org/10.1029/2010JG001365>, 2011.
- ter Braak, C. J. F. and Juggins, S.: Weighted averaging partial least squares regression (WA-PLS): an improved method for reconstructing environmental variables from species assemblages | SpringerLink, *Hydrobiologia*, 269/270, 485–502, 1993.

- Turner, M. G., Wei, D., Prentice, I. C., and Harrison, S. P.: The impact of methodological decisions on climate reconstructions using WA-PLS, *Quaternary Research*, 99, 341–356, <https://doi.org/10.1017/qua.2020.44>, 2021.
- van Andel, T. H., Zangger, E., and Demitrack, A.: Land Use and Soil Erosion in Prehistoric and Historical Greece, *Journal of Field Archaeology*, 17, 379–396, 1990.
- 1030 Walker, B., Holling, C. S., Carpenter, S. R., and Kinzig, A. P.: Resilience, Adaptability and Transformability in Social-ecological Systems, *E&S*, 9, art5, <https://doi.org/10.5751/ES-00650-090205>, 2004.
- Wanner, H.: Late-Holocene: Cooler or warmer?, *The Holocene*, 31, 1501–1506, <https://doi.org/10.1177/09596836211019106>, 2021.
- Watson, B. I., Williams, J. W., Russell, J. M., Jackson, S. T., Shane, L., and Lowell, T. V.: Temperature variations in the southern Great Lakes during the last deglaciation: Comparison between pollen and GDGT proxies, *Quaternary Science Reviews*, 182, 78–92, <https://doi.org/10.1016/j.quascirev.2017.12.011>, 2018.
- 1035 Weber, Y., Sinninghe Damsté, J. S., Zopfi, J., De Jonge, C., Gilli, A., Schubert, C. J., Lepori, F., Lehmann, M. F., and Niemann, H.: Redox-dependent niche differentiation provides evidence for multiple bacterial sources of glycerol tetraether lipids in lakes, *Proc. Natl. Acad. Sci. U.S.A.*, 115, 10926–10931, <https://doi.org/10.1073/pnas.1805186115>, 2018.
- 1040 Weijers, J. W. H., Schouten, S., Linden, M., Geel, B., and Sinninghe Damsté, J. S.: Water table related variations in the abundance of intact archaeal membrane lipids in a Swedish peat bog, *FEMS Microbiology Letters*, 239, 51–56, <https://doi.org/10.1016/j.femsle.2004.08.012>, 2004.
- Weijers, J. W. H., Schouten, S., Spaargaren, O. C., and Sinninghe Damsté, J. S.: Occurrence and distribution of tetraether membrane lipids in soils: Implications for the use of the TEX86 proxy and the BIT index, *Organic Geochemistry*, 37, 1680–
- 1045 1693, <https://doi.org/10.1016/j.orggeochem.2006.07.018>, 2006.
- Weijers, J. W. H., Schouten, S., van den Donker, J. C., Hopmans, E. C., and Sinninghe Damsté, J. S.: Environmental controls on bacterial tetraether membrane lipid distribution in soils, *Geochimica et Cosmochimica Acta*, 71, 703–713, <https://doi.org/10.1016/j.gca.2006.10.003>, 2007.
- Weijers, J. W. H., Panoto, E., van Bleijswijk, J., Schouten, S., Rijpstra, W. I. C., Balk, M., Stams, A. J. M., and Damsté, J. S.
- 1050 S.: Constraints on the Biological. Source(s) of the Orphan Branched Tetraether Membrane Lipids, *Geomicrobiology Journal*, 26, 402–414, <https://doi.org/10.1080/01490450902937293>, 2009.
- Wickham, H.: Data Analysis, in: *ggplot2: Elegant Graphics for Data Analysis*, edited by: Wickham, H., Springer International Publishing, Cham, 189–201, [https://doi.org/10.1007/978-3-319-24277-4\\_9](https://doi.org/10.1007/978-3-319-24277-4_9), 2016.
- Xiong, Q., Pan, K., Zhang, L., Wang, Y., Li, W., He, X., and Luo, H.: Warming and nitrogen deposition are interactive in shaping surface soil microbial communities near the alpine timberline zone on the eastern Qinghai–Tibet Plateau, southwestern China, *Applied Soil Ecology*, 101, 72–83, <https://doi.org/10.1016/j.apsoil.2016.01.011>, 2016.
- 1055 Yang, H., Pancost, R. D., Dang, X., Zhou, X., Evershed, R. P., Xiao, G., Tang, C., Gao, L., Guo, Z., and Xie, S.: Correlations between microbial tetraether lipids and environmental variables in Chinese soils: Optimizing the palaeo-reconstructions in semi-arid and arid regions, *Geochimica et Cosmochimica Acta*, 126, 49–69, <https://doi.org/10.1016/j.gca.2013.10.041>, 2014.

- 1060 Yang, H., Xiao, W., Słowakiewicz, M., Ding, W., Ayari, A., Dang, X., and Pei, H.: Depth-dependent variation of archaeal ether lipids along soil and peat profiles from southern China: Implications for the use of isoprenoidal GDGTs as environmental tracers, *Organic Geochemistry*, 128, 42–56, <https://doi.org/10.1016/j.orggeochem.2018.12.009>, 2019.
- Yurtsev, B.A.: Relics of the xerophyte vegetation of Beringia in northeastern Asia, in: *Paleoecology of Beringia*, edited by: Hopkins, D.M., Matthews Jr., J.V., Schweger, C.E., and Young, S.B., Academic Press, New York, 157–177, 1982.
- 1065 Zeng, Z., Chen, H., Yang, H., Chen, Y., Yang, W., Feng, X., Pei, H., and Welander, P. V.: Identification of a protein responsible for the synthesis of archaeal membrane-spanning GDGT lipids, *Nat Commun*, 13, 1545, <https://doi.org/10.1038/s41467-022-29264-x>, 2022.
- Zhao, B., Russell, J. M., Tsai, V. C., Blaus, A., Parish, M. C., Liang, J., Wilk, A., Du, X., and Bush, M. B.: Evaluating global temperature calibrations for lacustrine branched GDGTs: Seasonal variability, paleoclimate implications, and future directions, *Quaternary Science Reviews*, 310, 108124, <https://doi.org/10.1016/j.quascirev.2023.108124>, 2023.
- 1070 Zheng, Y., Li, Q., Wang, Z., Naafs, B. D. A., Yu, X., and Pancost, R. D.: Peatland GDGT records of Holocene climatic and biogeochemical responses to the Asian Monsoon, *Organic Geochemistry*, 87, 86–95, <https://doi.org/10.1016/j.orggeochem.2015.07.012>, 2015.
- Zheng, Y., Pancost, R. D., Naafs, B. D. A., Li, Q., Liu, Z., and Yang, H.: Transition from a warm and dry to a cold and wet climate in NE China across the Holocene, *Earth and Planetary Science Letters*, 493, 36–46, <https://doi.org/10.1016/j.epsl.2018.04.019>, 2018.
- 1075